Translational Diffusion of Fluorescent Proteins by Molecular Fourier Imaging Correlation Spectroscopy

Michael C. Fink,[†] Kenneth V. Adair,[†] Marina G. Guenza,*[†] and Andrew H. Marcus[†‡]

*Institute of Theoretical Sciences,[†]Department of Chemistry, University of Oregon, Eugene, Oregon; and [‡]Oregon Center for Optics, Eugene, Oregon

ABSTRACT   The ability to noninvasively observe translational diffusion of proteins and protein complexes is important to many biophysical problems. We report high signal/noise (≥ 250) measurements of the translational diffusion in viscous solution of the fluorescent protein, DsRed. This is carried out using a new technique: molecular Fourier imaging correlation spectroscopy (M-FICS). M-FICS is an interferometric method that detects a collective Fourier component of the fluctuating density of a small population of fluorescent molecules, and provides information about the distribution of molecular diffusivities. A theoretical analysis is presented that expresses the detected signal fluctuations in terms of the relevant time-correlation functions for molecular translational diffusion. Furthermore, the role played by optical orientational degrees of freedom is established. We report Fickian self-diffusion of the DsRed tetramer at short timescales. The long-time deviation of our data from Fickian behavior is used to determine the variance of the distribution of the protein self-diffusion coefficient. We compare our results to the expected outcomes for 1), a bi-disperse distribution of protein species, and 2), dynamic disorder of the host solvent.

INTRODUCTION

The translational motion of biomolecular species in complex environments is an important intermediate process in many biochemical reactions (1). Examples include the diffusive search preceding the assembly and disassembly of biomolecular complexes, the binding and release of substrates with receptors, and the switching of signal transduction proteins between active and passive states. In the cell, diffusion occurs through a suspension of macromolecules and lipids, many of which form molecular assemblies and compartments of varying complexity (2–4). The cell regulates its activities by coordinating the expression of proteins and other species that ultimately translate to their target sites. Clearly, measurements that monitor the motions of biological molecules through cell compartments can provide insight into subcellular organization and mechanisms of intracellular processes.

Because of the small volumes and opacity of most cell compartments, methods that characterize the movements of intracellular species require high signal sensitivity. Fluorescence methods are well suited to cell studies because they present strategies that allow the signal to be enhanced while suppressing background and noise. Furthermore, constructs of fluorescent proteins are often used to selectively label biomolecular species, which are expressed in living cells. In principle, single-particle tracking techniques can follow the motions of N labeled macromolecules through their local environments, and thus measure the dispersion of the observed motions. Indeed, live cell molecular imaging and tracking experiments have been reported with increasing frequency in recent years (5–9). Yet, despite their power and utility, all single-fluorophore experiments are subject to the disadvantages associated with detecting weak signals barely above ambient noise levels. The problem of low-signal-detection in the presence of noise is complex (10), but for our purposes we take the following simplified view. The limiting factors are: 1), reduced signal/noise (S/N, generally $\propto \sqrt{\text{signal}}$), which gives rise to 2), reduced temporal resolution (the time interval between successive measurements); and 3), reduced duration of a set of measurements (due to eventual photo-degradation of the fluorescent labels). These effects place practical constraints on the dynamic range accessible to a given experiment, as well as to its sensitivity to deviations from dynamically homogeneous behavior. In the cell, proteins interact with a myriad of intracellular species over a wide range of timescales, which ultimately gives rise to a broad distribution of dynamical behaviors. The purpose of this work is to present a new and alternative method to probe such distributions.

In this article, we demonstrate molecular Fourier imaging correlation spectroscopy (M-FICS) to characterize the translational dynamics of a small population of fluorescent proteins. Specifically, we present measurements in viscous solution of freely diffusing DsRed, a fluorescent protein that exists as a stable tetrameric complex at physiological and low salt concentrations, and over a wide pH range (11–13). We have chosen DsRed to demonstrate our method because of its exceptionally high extinction coefficient ($\varepsilon = 3 \times 10^5$ M^{-1} cm^{-1}) and fluorescence quantum yield ($q_F = 0.79$) (14). In our experiments, the tetrameric complex is suspended in 95% glycerol/water mixtures. These studies are carried out using a sensitivity-enhanced version of our recently developed FICS technique (15–17). M-FICS is a complementary method to single-molecule imaging because it exchanges unneeded spatial information for improved S/N, temporal resolution, and dynamic range (16). Similar to single-molecule spectroscopy,

M-FICS has the ability to characterize distributions of molecular parameters. Our experiments monitor the emissive fluctuations resulting from the spatial overlap of an optically resonant intensity interference fringe pattern and a small population of diffusing chromophores (see Fig. 1). The phase of the excitation pattern is continuously swept, resulting in a modulated fluorescence signal. We record the phase and amplitude of the signal using a lock-in amplifier to determine the complex-valued Fourier transform of the fluctuating (real-valued) local chromophore density, defined at the wave vector of the optical grating. From these data, we construct the intermediate scattering function (ISF), which provides a quantitative description of the protein molecular displacements. Furthermore, we characterize the departure of the ISF from Fickian behavior in terms of the variance of the distribution of protein diffusivity.

FICS has been used to study dense suspensions of fluorescently labeled poly(styrene) beads (17) and mitochondrial membranes in living cells (15,18). It has been used to decompose the dynamics of a dilute binary colloidal fluid, and to separately determine the relative and collective contributions of the component species (19).

In all previous FICS studies, the number of fluorescent chromophores that decorate each particle is large ($\geq 10^3$). Such systems are optically isotropic since the absorption and emission probabilities are independent of particle orientation. In this case, the fluctuating signal contains contributions due solely to particle center-of-mass motions. A different situation arises when the particles are themselves optically anisotropic molecules. The system then has a continually fluctuating instantaneous anisotropy, due to the tensorial relationship between the polarization of the excited state population and that of the exciting laser field. If the polarization of the excitation and emission fields is specified, the signal can, in principle, contain steady state and time-dependent contributions from molecular orientational degrees of freedom. Future polarization-selective M-FICS studies could be used to separate the effects of transition dipole reorientation from center-of-mass degrees of freedom. In the present work, optical anisotropy fluctuations either occur on a much shorter timescale than the shortest experimental integration period

($\sim$5 ms), or are effectively removed using a magic-angle polarization scheme. Thus, optical anisotropy fluctuations contribute only a time-averaged constant factor to the signal. In principle, even with magic-angle detection, there could exist signal contributions due to excited state population dynamics, such as intersystem crossing to long-lived non-radiative dark states. Such photoconversion phenomena have been observed to occur in DsRed on sub-millisecond timescales, and at excitation intensities much higher than those applied in the current studies (a factor $\geq 10^4$) (20–22). For the experiments presented below, we show that the signal fluctuations are dominated by contributions from molecular center-of-mass displacements and are unaffected by photoconversion processes. Our results suggest that our technique is well suited for studies of molecular diffusion.

The remainder of this article is organized in the following manner. In Theoretical Background, we relate molecular density fluctuations to the relevant time correlation functions for self-diffusion. In Experimental Methods, we explain the M-FICS method, including instrumental and technical details that were implemented to achieve the necessary sensitivity. In Results and Discussion, we present our results.

THEORETICAL BACKGROUND

Molecular fluctuations and the self-intermediate scattering function

In the following M-FICS experiments, we study the fluctuating emission from the fluorescent protein, DsRed. The protein molecules, which are suspended under dilute conditions in an unlabeled host fluid, are at equilibrium and randomly exchange momentum with the surroundings (23). We treat the system as N Brownian particles in a macroscopic (illumination) volume V, with mean number density $\bar{n} = N/V$. Because our measurements are sensitive only to molecular center-of-mass displacements (see Introduction and following sections), we focus our discussion on the center-of-mass coordinates; however, in Experimental Methods we discuss the potential role played by orientational degrees of freedom.
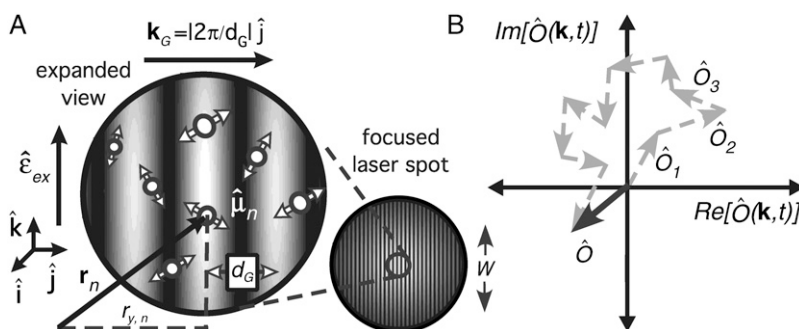

FIGURE 1 (*A*) Schematic of the M-FICS experimental geometry. A small population of optically resonant molecular dipoles is illuminated by a focused laser interference pattern (represented as gray-scale bars). The transverse beam profile is Gaussian with a waist, $w \sim 100~\mu$m. The expanded view shows three fringes across the center of the beam profile; the minimal fringe number used is $\sim$30. A molecular configuration is specified (in three dimensions) by the set of vector positions $\{\mathbf{r}_1, \mathbf{r}_2, \ldots, \mathbf{r}_N\}$ and orientations $\{\hat{\mu}_1, \hat{\mu}_2, \ldots, \hat{\mu}_N\}$. The fluorescence signal depends on fluctuations of the local orientational density, defined by Eq. 12. (*B*) At any instant, a static configuration of molecular dipoles is uniquely described by a sum of phasors in the complex plane, as described by Eq. 15.

A local fluctuation from the mean number density is given by

$$\delta n(\mathbf{r}, t) = n(\mathbf{r}, t) - \bar{n} \qquad (1)$$

where $n(\mathbf{r}, t) = \sum_{i=1}^{N} \delta[\mathbf{r} - \mathbf{r}_i(t)]$ is the number density operator for fluorescent molecules at time t, and $\delta(x)$ is the Dirac delta function.

As explained below, the measurement observable in an M-FICS experiment is proportional to a Fourier component of the density fluctuation of the fluorescent molecules, $\delta n(\mathbf{r}, t)$, with a specified wave vector, $\mathbf{k}$. This $\mathbf{k}$-space number density operator is given by the spatial Fourier transform,

$$\hat{N}(\mathbf{k}, t) = \int_{-\infty}^{\infty} d^3 r\, e^{i\mathbf{k}\cdot\mathbf{r}} \delta n(\mathbf{r}, t) = \sum_{i=1}^{N} e^{i\mathbf{k}\cdot\mathbf{r}_i(t)} - N\delta(\mathbf{k}). \quad (2)$$

Since $\delta n(\mathbf{r}, t)$ is real-valued, $\hat{N}^*(\mathbf{k}, t) = \hat{N}(-\mathbf{k}, t)$. We may therefore expand $\delta n(\mathbf{r}, t)$ in terms of its Fourier components,

$$\delta n(\mathbf{r}, t) = \frac{(2\pi)^3}{V} \int_{-\infty}^{\infty} d^3 k\, \hat{N}(\mathbf{k}, t) e^{-i\mathbf{k}\cdot\mathbf{r}}. \qquad (3)$$

Measurement of $\hat{N}(\mathbf{k}, t)$ allows us to calculate its auto-correlation function, called the intermediate scattering function (ISF),

$$S(\mathbf{k}, \tau) = \frac{1}{N} \langle \hat{N}^*(\mathbf{k}, t)\hat{N}(\mathbf{k}, t + \tau)\rangle$$
$$= \frac{1}{N} \sum_{i=1}^{N} \sum_{j=1}^{N} \langle \exp\{i\mathbf{k}\cdot[\mathbf{r}_i(t) - \mathbf{r}_j(t + \tau)]\}\rangle. \quad (4)$$

In Eq. 4, the angle brackets indicate an average over all starting times, t, and $S(\mathbf{k}, \tau)$ remains nonzero for τ within the time interval over which successive center-of-mass configurations are correlated. The ISF quantifies the degree of correlation between the Fourier component of the local density fluctuation at time t with that at time $t + \tau$. It is related by Fourier transformation to the van Hove space-time correlation function, $G(\mathbf{r}, \tau)$ (24),

$$S(\mathbf{k}, \tau) = (2\pi)^3 \bar{n} \int_{-\infty}^{\infty} G(\mathbf{r}, \tau) e^{-i\mathbf{k}\cdot\mathbf{r}} d\mathbf{r}, \qquad (5)$$

where

$$G(\mathbf{r}, \tau) = \frac{1}{N} \left\langle \sum_{i=1}^{N} \sum_{j=1}^{N} \delta[\mathbf{r} + \mathbf{r}_i(t) - \mathbf{r}_j(t + \tau)] \right\rangle. \qquad (6)$$

The van Hove function (Eq. 6) represents the conditional probability that a molecule will be found at position $\mathbf{r}$ at time τ, given that either the same or a different molecule was at position $\mathbf{r} = 0$ at time $\tau = 0$. The ISF (Eq. 4) contains all of the information necessary to characterize the dynamics of the fluid system and is the natural starting point for theories of the liquid state (24).

We now specialize to the current situation: measurements performed under dilute conditions (~ 10 nM). Because the mean separation between molecules $\bar{d}_0 = (\bar{n})^{-\frac{1}{3}}(\sim 550$ nm) is much

larger than any natural length scale of the system, the cross-terms in Eq. 4 representing distinct molecule-molecule interactions contribute minimally to the sum, leaving the self-terms to dominate (24–26). Thus, in the dilute limit, Eq. 4 reduces to

$$F_s(\mathbf{k}, \tau) = \langle \exp\{i\mathbf{k}\cdot[\mathbf{r}(t) - \mathbf{r}(t + \tau)]\}\rangle. \qquad (7)$$

$F_s(\mathbf{k}, \tau)$ is called the self-part of the ISF; it describes the temporal correlation of self-displacements of the molecular center-of-mass. Equation 7 can be further simplified by using the Gaussian model for single particle displacements (25). The Gaussian model is a good approximation when the measurement timescale is large compared to the decay time of the velocity autocorrelation function. In this case, the self-displacement vector $\Delta\mathbf{r}(\tau) = \mathbf{r}(t) - \mathbf{r}(t + \tau)$ behaves as a Gaussian random variable, and the self-ISF becomes

$$F_s(\mathbf{k}, \tau) = \exp\{-k^2\langle\Delta\mathbf{r}^2(\tau)\rangle/6\} = \exp[-k^2 D_s\tau], \quad (8)$$

where we have assumed the Fickian relationship between the mean-square displacement $\langle\Delta\mathbf{r}^2(\tau)\rangle$ and the translational self-diffusion coefficient D_s. For a fluid of mono-disperse spherical particles undergoing Fickian dynamics, the self-diffusion coefficient is given by the Stokes-Einstein relation, $D_S = k_B T/6\pi\eta a$, where k_B is the Boltzmann constant, T is the temperature, η is the viscosity of the medium, and a is the molecular hydrodynamic radius.

Equation 8 predicts that the ISF decays exponentially in time and as a Gaussian with increasing wave number. One often observes deviations from Fickian behavior when considering self-diffusion of polydisperse systems (25) or of identical particles immersed in dynamically heterogeneous media (27). Various particles then exhibit a distribution $\Omega(\Gamma)$ of dynamical behaviors, which may reflect differences in particle size, shape, or local environment. In this case, the observed ISF reflects a weighted average over this distribution

$$F_s(k, \tau) = \int_0^{\infty} d\Gamma\, \Omega(\Gamma) e^{-\Gamma\tau}, \qquad (9)$$

where $\Gamma = k^2 D_s$. In principle, Laplace inversion of the measured ISF could determine $\Omega(\Gamma)$, although this would require exceptionally high S/N. It is less demanding to determine low-order moments of the distribution. An expansion of Eq. 9 at short time yields the second-order truncated cumulant approximation (28–30),

$$F_s(k, \tau) = \exp[-k^2\bar{D}_s\tau]\left\{1 + \frac{1}{2}Q\bar{D}_s^2 k^4\tau^2 + O(\tau^3)\right\}, \quad (10)$$

where the parameter $Q = \{[\langle D_s^2\rangle/\bar{D}_s^2] - 1\}$ is a measure of the dispersion of the underlying distribution. We return to Eqs. 8 and 10 in Results and Discussion.

EXPERIMENTAL METHODS

Molecular-FICS

M-FICS is an extension of the FICS method introduced by Grassman et al. (16,17) to study diffusion of uniformly labeled fluorescent particles. Here,

we have greatly improved its sensitivity to detect the center-of-mass fluctuations of a small number of diffusing molecules. An important aspect of M-FICS is that the molecular motions of interest occur on timescales much longer than the excited state lifetime. Fluctuations of the steady-state fluorescence then reflect slow changes in molecular coordinates. We present measurements on dilute viscous solutions ($\bar{n} \sim 10$ nM) of DsRed in ~95% glycerol/water. The mean number of molecules is $N = \bar{n}V \simeq 470,000$, in a volume $V \simeq 78,500~\mu m^3$ (as described below). Our measurements span a range of time (10^{-3}–10^1 s) and distance (1.2–3.5 μm) scales sufficient to characterize the translational diffusion under these conditions.

We use a continuous-wave laser to create an intensity interference fringe pattern that illuminates a fluid sample positioned in a fluorescence microscope (Fig. 1 A). The laser resonantly excites an electronic transition of the molecules, which we treat here simply as N molecular dipoles. Molecules are indicated schematically in Fig. 1 A as white disks, whose center-of-mass and transition dipole orientation coordinates are specified by the vectors $\{\mathbf{r}_1, \mathbf{r}_2, \ldots, \mathbf{r}_N\}$ and $\{\hat{\mu}_1, \hat{\mu}_2, \ldots, \hat{\mu}_N\}$, respectively. The vectors $\hat{\mu}_i$ collectively represent the absorption ($^a\hat{\mu}_i$) and emission ($^e\hat{\mu}_i$) transition dipole moments, which are fixed in the molecular frame. Since the fringe spacing d_G is small compared to the focused laser beam waist w (~100 μm), we approximate the intensity profile as an infinite plane wave (31,32)

$$I_{ex}(y, \phi) = I_0\{1 + \cos[k_G y + \phi(t)]\}. \qquad (11)$$

We have chosen a right-handed coordinate system with the wave vector of the optical grating oriented parallel to the y axis, $\mathbf{k}_G = (2\pi/d_G)\hat{\mathbf{j}}$, and the electric field polarization parallel to the z axis, $\hat{\varepsilon}_{ex} = |\hat{\varepsilon}_{ex}|\hat{\mathbf{k}}$. We also define a time-varying phase $\phi(t) = \omega_G t + \varphi_G$, where ω_G is an angular sweep frequency ($\nu_G = \omega_G/2\pi \approx 10$ MHz), φ_G is a constant phase, and I_0 is a constant intensity.

A local fluctuation of the chromophore coordinates is described by the function

$$\delta o(\mathbf{r}, t) = \sum_{i=1}^{N} A_i[\hat{\mu}_i(t)]\delta[\mathbf{r} - \mathbf{r}_i(t)] - \bar{n}\bar{A}, \qquad (12)$$

where $A_i[\hat{\mu}_i(t)]$ is a slowly fluctuating molecular intensity, proportional to the ith molecule's excitation/emission probability, and $\bar{A} = \frac{1}{N}\langle\sum_{i=1}^{N} A_i[\hat{\mu}_i(t)]\rangle$ is its time-averaged value. We assume that the molecular intensities fluctuate on timescales longer than the experimental integration period (~5 ms) and the fluorescence lifetime ($\tau_F \sim 3.5$ ns) (33). Furthermore, the intensities $A_i[\hat{\mu}_i(t)]$ are explicit functions of the orientational coordinates, since they depend on transition dipole coupling to the excitation and emission fields. To streamline our notation, we write the intensities as explicit functions of time, $A_i(t)$. Equation 12 thus describes the fluctuation of the optical orientational density of the system, as each molecule contributes a center-of-mass coordinate weighted by its orientation-dependent intensity. On the experimental timescale, the steady-state molecular intensities fluctuate due to slow motions of the molecular transition dipoles.

At any instant, the emitted fluorescence $I_f(t,\phi)$ is proportional to the excited state population generated by the spatial overlap between the laser intensity $I_{ex}(y,\phi)$ and the local orientational density $o(\mathbf{r}, t) = \delta o(\mathbf{r}, t) + \bar{o}$, defined according to Eq. 12:

$$I_f(t, \phi) = \int d^3r\, I_{ex}(y, \phi)o(\mathbf{r}, t). \qquad (13)$$

The form of Eq. 13 shows that the instantaneous fluorescence is proportional to $\hat{O}(\mathbf{k}_G, t)$, the Fourier component of the local orientational density evaluated at $\mathbf{k} = \mathbf{k}_G$.

We sweep the phase of the grating, $\phi(t)$, across the sample at the velocity $v_G = \omega_G / k_G$ (~10 m s^{-1}), orders of magnitude faster than the average speed of molecular diffusion. We thus generate a time-varying excited state population that is proportional to the emitted fluorescence. We use the waveform that sweeps the grating as the reference for lock-in detection. The carrier frequency of this reference (10 MHz) sets the upper limit to the experimentally accessible bandwidth. Signal fluctuations that occur within

the experimental bandwidth give rise to a slowly varying envelope function that multiplies the carrier signal. We take advantage of the separation in timescales between the signal fluctuations and the inverse modulation frequency by writing the signal as a two-dimensional function of the slow variable t, and the fast carrier phase, $\phi(t) = \omega_G t + \varphi_G$. The resulting fluorescence intensity has the form (16,17)

$$I_f(t, \phi) = I_0\{\hat{O}(\mathbf{k}_G = 0) + |\hat{O}(\mathbf{k}_G, t)|\cos[\phi + \gamma(\mathbf{k}_G, t)]\}. \qquad (14)$$

Equation 14 shows that the signal consists of two parts; a stationary (dc) background and a time-varying (ac) component. The background is proportional to the mean number of optically oriented molecules contained in the illumination volume (i.e., $\hat{O}(\mathbf{k}_G = 0) = \bar{A}\bar{n} \propto N$). The ac signal has amplitude, $|\hat{O}|$, and phase, γ, proportional to those of the complex Fourier component of the orientational density fluctuation

$$\hat{O}(\mathbf{k}_G, t) = \sum_{i=1}^{N} A_i(t)\exp[i\mathbf{k}_G \cdot \mathbf{r}_i(t)] \equiv |\hat{O}|\exp(i\gamma). \qquad (15)$$

We use a lock-in amplifier to demodulate the signal in terms of the in-phase and in-quadrature components, $\mathrm{Re}\hat{O} = |\hat{O}|\cos\gamma$ and $\mathrm{Im}\hat{O} = |\hat{O}|\sin\gamma$, respectively (17). As depicted in Fig. 1 B, at any instant, the Fourier component, $\hat{O}$, is a vector sum of N single molecule terms. Each molecule contributes an intensity, A_i, and a phase, $\gamma_i = \mathbf{k}_G \cdot \mathbf{r}_i = k_G r_{y,i}$, to the measured value of $\hat{O}$. Because $\mathbf{k}_G$ points in the direction of the y-axis, only the y-projections of the $\mathbf{r}_i$ values contribute to the molecular phases. Fig. 1 B illustrates the relationship between the detected signal, $\hat{O}$, and the center-of-mass positions $\mathbf{r}_i$ of the labeled species (see Eq. 15). If the molecular positions are randomly distributed, the signal amplitude scales roughly as the end-to-end vector of a Gaussian random variable, i.e., $|\hat{O}| \propto N^{1/2}$. In this limit, the ratio of the signal modulation amplitude to its mean value scales as the number density fluctuation, i.e., $|\hat{O}|/\hat{O}(\mathbf{k} = 0) \propto N^{-1/2}$.

The vector $\hat{O}$ fluctuates in the complex plane due to collective orientational and translational motions of the molecules. We determine the time- and wave-vector dependence of $\hat{O}$ to construct the ISF defined by Eq. 4. A general expression for the time correlation function is

$$S(\mathbf{k}_G, \tau) = \frac{1}{N}\langle\hat{O}^*(\mathbf{k}_G, t)\hat{O}(\mathbf{k}_G, t + \tau)\rangle$$
$$= \frac{1}{N}\sum_i^N\sum_j^N\langle A_i(t)A_j(t + \tau)\exp\{i\mathbf{k}_G \cdot [\mathbf{r}_i(t) - \mathbf{r}_j(t + \tau)]\}\rangle. \qquad (16)$$

We further define the normalized ISF, $F(\mathbf{k},\tau) = S(\mathbf{k},\tau)/S(\mathbf{k})$, where $S(\mathbf{k}) = S(\mathbf{k},\tau = 0)$ is called the static structure function.

At this stage, we make the following assumptions: 1), that the center-of-mass positions of different molecules are statistically independent, and 2), that there is no coupling between rotational and translational diffusion. This is consistent with a dilute solution of molecules undergoing Brownian diffusion (far above the glass transition temperature and neglecting pairwise particle interactions). Equation 16 then simplifies to

$$S(\mathbf{k}_G, \tau) = \frac{1}{N}\sum_{i=1}^N\langle A_i(t)A_i(t + \tau)\rangle \cdot \langle\exp i\mathbf{k}_G \cdot [\mathbf{r}_i(t) - \mathbf{r}_i(t + \tau)]\rangle$$
$$= \langle A(t)A(t + \tau)\rangle \cdot F_s(\mathbf{k}_G, \tau). \qquad (17)$$

Equation 17 shows that the ISF is the product of two terms. The first, $\langle A(t)A(t + \tau)\rangle$, depends on molecular optical orientational dynamics, and is independent of $\mathbf{k}_G$. The second term is the self-part of the ISF, $F_s(\mathbf{k}_G,\tau)$ (defined by Eq. 7), which depends only on the molecular center-of-mass

positions. For the purposes of this work, we wish to isolate the translational dynamics from possible anisotropy contributions to the signal. This is accomplished by selecting the polarization of the fluorescence using an analyzer oriented at the magic-angle (MA = 54.7°) relative to the excitation polarization. We discuss the functional form of $\langle A(t)\, A(t + \tau)\rangle$ and its dependence on optical orientational dynamics in the next section.

Orientational time-correlation function

The molecular intensities, $A_i(t)$, are proportional to the square of the projections of the absorption and emission transition dipole moments onto the excitation and detection electric fields (25,34,35), $A_i \propto [^a\hat{\mu}_i \cdot \hat{\varepsilon}_{\text{ex}}]^2$ $[^e\hat{\mu}_i(t) \cdot \hat{\varepsilon}_{\text{det}}]^2$. The intensities therefore depend on the laboratory fixed polarizer and analyzer orientations, and the probability distribution of the molecular transition dipoles. If we used a long focal length lens for detection, the polarized intensity transmitted through the analyzer would be the square of the projections of those dipoles that emit rays parallel to the optic axis. However, we must account for the more complicated situation associated with the high numerical aperture (NA) objective lens used in the M-FICS geometry (see Fig. 2 A). We place the analyzer behind the objective's back-aperture, so that the polarized intensity is the sum of the squared projections of all rays emitted over the solid angle subtended by the lens. Axelrod treated this problem in detail, showing that the polarized emission from a single dipole contains contributions from field projections onto all three orthogonal laboratory frame axes (36,37). A straightforward calculation (see Appendix A) shows that the molecular intensity transmitted through the analyzer, oriented at the magic-angle (MA = 54.7°) relative to $\hat{\varepsilon}_{\text{ex}}$, is

$$A_i^{\text{MA}}(t; t')$$
$$= \kappa^{\text{MA}}\left\{K_{\text{a}} + K_{\text{b}} + K_{\text{c}} + \frac{2}{5}\langle P_2[^a\hat{\mu}_i(t') \cdot^e \hat{\mu}_i(t)]\rangle(K_{\text{b}} - K_{\text{a}})\right\},$$
(18)

where the intensity at time t is conditionally dependent on the molecule being excited at time $t' < t$. In Eq. 18, the proportionality constant κ_{MA} accounts for the absorption cross-section, fluorescence quantum yield, and light collection efficiency of the experimental setup. The function $P_2(x) = (3x^2 - 1)$ is the second Legendre polynomial, which appears in the instantaneous fluorescence anisotropy $\frac{2}{5}\langle P_2[^a\hat{\mu}_i(t') \cdot^e \hat{\mu}_i(t)]\rangle$; its argument is the projection of the absorption transition dipole moment (at the time t' of excitation) onto the emission transition dipole moment (at the detection time t). The constants K_{a}, K_{b}, and K_{c} depend on the numerical aperture of the objective lens:

$$K_{\text{a}} = \frac{1}{6}(2 - 3\cos\sigma_0 + \cos^3\sigma_0)(1 - \cos\sigma_0)^{-1}, \quad (19\text{a})$$

$$K_{\text{b}} = \frac{1}{24}(1 - 3\cos\sigma_0 + 3\cos^2\sigma_0 - \cos^3\sigma_0)(1 - \cos\sigma_0)^{-1},$$
(19b)

$$K_{\text{c}} = \frac{1}{8}(5 - 3\cos\sigma_0 - \cos^2\sigma_0 - \cos^3\sigma_0)(1 - \cos\sigma_0)^{-1},$$
(19c)

where the angle σ_0 is defined by NA $= n_0 \sin\sigma_0$, and n_0 is the refractive index of the medium. We note that in the small aperture limit, $\sigma_0 \to 0$, $K_{\text{c}} \to 1$, and $K_{\text{a}}, K_{\text{b}} \to 0$, such that the magic-angle intensities become independent of the anisotropy as expected, i.e., $A_i^{\text{MA}} \to \kappa^{\text{MA}}$ (38). For our experiments, NA = 1.4, $n_0 = 1.518$, and $\sigma_0 = 67.3°$, for which $K_{\text{a}} = 0.2440$, $K_{\text{b}} = 0.0157$, and $K_{\text{c}} = 0.7404$. Thus, the effect of high NA is to mix into the magic-angle intensity a finite, albeit small, anisotropy contribution.

During the course of a measurement, the detected signal is integrated over a short period. For a measurement performed at time t, the intensities that contribute to the signal represent the sum of all prior absorption events that can lead to emission at this time. We define a normalized function
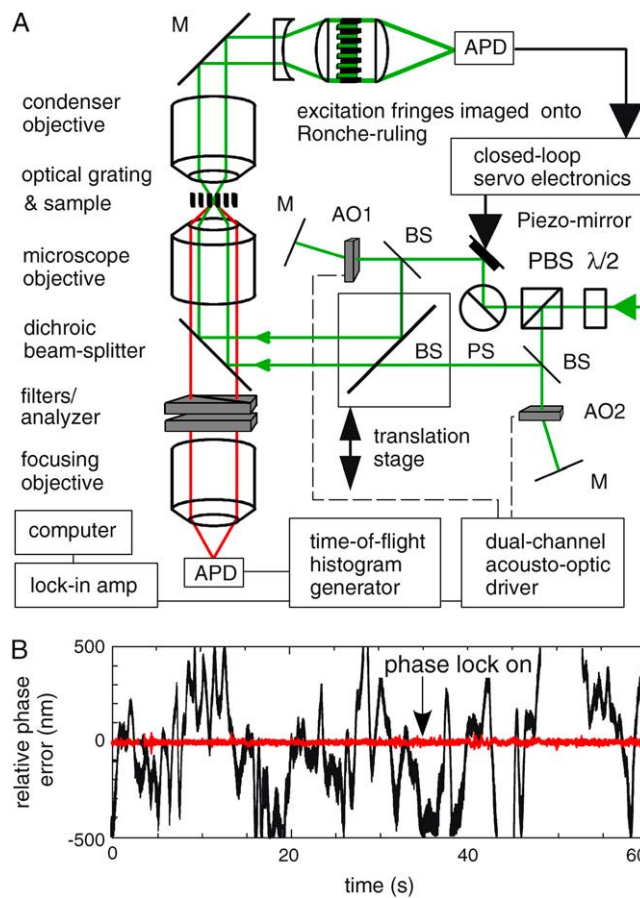

FIGURE 2 (A) Schematic diagram of the experimental setup for M-FICS (described in text). (Abbreviations have the following meanings: *APD*, amplified photo-diode; *M*, mirror; *AO1(2)*, Bragg cell 1 (2); *BS*, beam splitter; *PBS*, polarizing beam-splitter; *PS*, periscope; and λ/2, half-wave plate.) A spatially and temporally modulated interference fringe pattern illuminates a sample positioned at the object plane of a fluorescence microscope. The pattern is produced using a Mach-Zehnder interferometer (*MZI*) with acousto-optic Bragg cells placed in the two beam paths. The image of the excitation pattern is magnified and relayed through a Ronche ruling, and the resulting temporally modulated intensity is focused onto an APD. The APD signal is used as negative feedback to a servo, which corrects the relative path lengths of the MZI (via a piezo-mounted mirror), to minimize passive phase instabilities. The weak fluorescence from the sample is collected in an epi-configuration, filtered according to frequency and polarization (at the magic-angle), and detected using a second photon-counting APD module. The signal is processed using a time-of-flight histogram generator (described in Appendix B). A lock-in amplifier demodulates the resulting analog output. (B) A typical time-course for the random phase error (RPE) with feedback loop engaged (*red*, RMS RPE = 4 nm) and disengaged (*black*, RMS RPE = 300 nm), measured for $d_{\text{G}} = 1.0\ \mu$m.

$P_{\text{c}}(t - t')dt'$ as the probability that a molecule emits a photon at time t, given that it was excited at time t' (35). The convolved intensities are then

$$A_i^{\text{MA}}(t) = \int_{-\infty}^{t} P_{\text{c}}(t - t')A_i^{\text{MA}}(t; t')dt'. \quad (20)$$

For a system characterized by one fluorescence lifetime τ_{F}, we have $P_{\text{c}}(t - t') = \exp[-(t - t')/\tau_{\text{F}}]/\tau_{\text{F}}$ (35). Because the experimental integration time (~5 ms) is much larger than τ_{F} (~3.5 ns) (33), all absorption/emission

events appear instantaneous in comparison. We may therefore take the limit $P_c(t - t') \to \delta(t - t')$, and using Eqs. 18–20 obtain

$$A_i^{\mathrm{MA}}(t) = \kappa^{\mathrm{MA}}[1.0001 - 0.0913\,\bar{P}_{2,i}(t)]. \qquad (21)$$

In Eq. 21, we have used the numerical aperture values given by the expressions in Eq. 19, and have defined

$$\bar{P}_{2,i}(t)$$
$$= \int_{-\infty}^{t} I_0 e^{-(t-t')/\tau_F} P_{2,i}[{}^a\hat{\mu}_i(t') \cdot {}^e \hat{\mu}_i(t)]dt' \bigg/ \int_{-\infty}^{t} I_0 e^{-(t-t')/\tau_F}dt' \qquad (22)$$

as the (slowly) fluctuating steady-state fluorescence anisotropy of the ith molecule. We regard $\bar{P}_{2,i}(t)$ as a stochastic variable that fluctuates about its mean value $\bar{P}_2$ given by the integral of the P_2 time-correlation function

$$\bar{P}_2 = \int_0^{\infty} I_0 e^{-t/\tau_F} P_2({}^a\hat{\mu}_i \cdot {}^e \hat{\mu}_i)dt \bigg/ \int_0^{\infty} I_0 e^{-t/\tau_F}. \qquad (23)$$

For example, a symmetric top molecule undergoing rotational Brownian diffusion has $P_2({}^a\hat{\mu}_i \cdot {}^e \hat{\mu}_i) = \exp(-6D_R t)$, and Eq. 23 yields the Perrin equation, $\frac{2}{5}\bar{P}_2 = \frac{2}{5}[1+6D_R\tau_F]^{-1}$, where the rotational diffusion coefficient is given by $D_R = k_B T/8\pi\eta a^3$ (23,38).

Using Eq. 21, we calculate the two-point orientational time-correlation function

$$\langle A^{\mathrm{MA}}(t)A^{\mathrm{MA}}(t + \tau)\rangle = (\kappa^{\mathrm{MA}})^2\{1 - 0.1826\bar{P}_2 + 0.0083\langle\bar{P}_2(t)\bar{P}_2(t+\tau)\rangle\}, \qquad (24)$$

where we have adjusted the proportionality factor to make the leading term in the parentheses equal to one. Equation 24 expresses $\langle A^{\mathrm{MA}}(t)A^{\mathrm{MA}}(t+\tau)\rangle$ in terms of the (stationary) mean fluorescence anisotropy, $\bar{P}_2$, and its two-point time-correlation function $\langle\bar{P}_2(t)\bar{P}_2(t+\tau)\rangle$. While $\bar{P}_2$ describes the average rotation time of the molecular transition dipoles on the timescale of the fluorescence lifetime, $\langle\bar{P}_2(t)\bar{P}_2(t+\tau)\rangle$ describes the regression of spontaneous fluctuations of the $\bar{P}_2$ function about its mean value, i.e., $\delta\bar{P}_2(t) = \sum_{i=1}^{N}\bar{P}_{2,i}(t) - \bar{P}_2$. We note that the two-point time correlation function $\langle\bar{P}_2(t)\bar{P}_2(t+\tau)\rangle$ is more precisely defined as a four-point time correlation function (with $t_1 < t_2 \ll t_3 < t_4$),

$$\langle P_2[{}^a\hat{\mu}(t_1) \cdot {}^e \hat{\mu}(t_2)]P_2[{}^a\hat{\mu}(t_3) \cdot {}^e \hat{\mu}(t_4)]\rangle, \qquad (25)$$

over which the time intervals between adjacent excitation and detection events, $t_2 - t_1$ and $t_4 - t_3$, have been integrated in Eq. 22. Multitime correlation functions of this type are often discussed in the context of nonlinear spectroscopic measurements, and can potentially contain information about slow intramolecular structural dynamics or even pairwise molecular interactions. As a simple example, if the optical orientational fluctuations were due solely to isotropic rotational diffusion, one can show by solving the rotational Smoluchowski equation that $\langle\bar{P}_2(t)\bar{P}_2(t+\tau)\rangle = \langle\bar{P}_2^2\rangle\exp(-6D_R t)$, where $\langle\bar{P}_2^2\rangle = 2/5$ is the mean-square anisotropy for an initially isotropic distribution (23). Making the above substitutions into Eq. 24, we obtain

$$\langle A^{\mathrm{MA}}(t)A^{\mathrm{MA}}(t + \tau)\rangle = (\kappa^{\mathrm{MA}})^2[1 - 0.187(1 + 6D_R\tau_F)^{-1} + 0.0035\exp(-6D_R\tau)]. \qquad (26)$$

Note that the time-dependent term in Eq. 26 contributes just ~0.35% of the total amplitude. Thus, $\langle A^{\mathrm{MA}}(t)A^{\mathrm{MA}}(t+\tau)\rangle$ is dominated by the stationary terms, and the effect of high NA is to rescale this value from $(\kappa^{\mathrm{MA}})^2 \to (\kappa^{\mathrm{MA}})^2[1 - 0.1826(1+6D_R\tau_F)^{-1}]$.

M-FICS instrumentation

M-FICS studies of molecular diffusion require very dilute samples (~10 nM). We must therefore detect weak fluorescence signals against a significant noise background. With this in mind, we modified the original

FICS apparatus, described by Grassman et al. (16–18), to detect small numbers of diffusing fluorescent molecules. Our modifications include:

1. Phase modulation at high frequency ($\nu_G \sim 10$ MHz).
2. Reduction of our instruments sensitivity to ambient mechanical vibrations.
3. Introduction of single-photon-counting into our phase-synchronous-detection scheme.

Interferometer

In Fig. 2 A, we show a schematic diagram of the M-FICS apparatus. The excitation fringe pattern is produced at the sample plane of a fluorescence microscope (model No. TE-2000U; Nikon, Tokyo, Japan) using a modified Mach-Zehnder interferometer. The frequency-doubled continuous-wave output (532 nm) of a low-noise, diode-pumped Nd:YAG laser (Compass model No. 215M, 50 mW, shown in *green*; Coherent, Santa Clara, CA) is isolated from trace fundamental light (1064 nm) using a pair of harmonic separators (not shown; model No. BSR-51-1037, CVI International, Norfolk, VA), and from trace 780-nm diode pump light using a laser line filter (model No. 520DF40; Omega Optical, Brattleboro, VT). The beam is split by a polarizing beam-cube, with the resulting two beams directed along equivalent interferometer arms (indexed 1 and 2). A periscope rotates the polarization of beam-1 times 90° so that it is parallel to that of beam-2. The relative intensity of the two arms is balanced using a half-wave plate. Each beam path contains an acousto-optic (AO) Bragg cell, labeled AO1 (model No. 15150-2; NEOS Technologies, Melbourne, FL) and AO2 (model No. 46200-2, NEOS Technologies) with 100-μm active areas. A digital, phase-locked, dual-channel driver (model No. N64020-250; NEOS Technologies) supplies distinct frequency waveforms to the two AO cells ($\nu_{BC1} = 175$ MHz and $\nu_{BC2} = 180$ MHz). A custom-built waveform mixer generates a well-defined difference frequency signal from the outputs of the driver. This difference signal serves as the reference (with phase φ_{ref}) for phase-synchronous-detection. Each AO imparts a time-varying phase shift to its respective beam. The first-order Bragg peak is spatially filtered and retro-reflected for a second pass, effectively Doppler-shifting the optical frequencies by $2\nu_{BC1}$ and $2\nu_{BC2}$. The electric fields of the two beams are given by $\mathbf{E}_{1(2)} = \varepsilon_0 \exp i[\mathbf{k}_{1(2)} \cdot \mathbf{r} - 2\pi\nu_{\mathrm{laser}}t - 4\pi\nu_{BC1(2)}t + \varphi_{1(2)}]$, where $\mathbf{k}_{1(2)}$ is the wave vector of beam-1 (or -2). Cylindrical lenses (not shown) are used to correct for astigmatism introduced by the Bragg cells. The beam arms are made parallel using a beam-splitter mounted to a translation stage, and reflected by a dichroic mirror (model No. C-36159, 96321 M TRITC HQ, Nikon). The collimated beam diameters are adjusted using a telescope (not shown) to underfill the back aperture of a polarization-preserving oil-immersion objective lens (Plan Apo, 100×, NA 1.4, and w.d. 0.13 mm; Nikon), so that the focused beam waist at the sample is $w \sim 100$ μm. The beams cross at the focal plane of the objective to create an intensity interference fringe pattern that runs parallel to the y axis. The resulting intensity is the square modulus of the total electric field, $\mathbf{E}_1 + \mathbf{E}_2$:

$$I_{\mathrm{ex}}(y,\phi) = 2|\varepsilon_0|^2\{1 + \cos[|\mathbf{k}_2 - \mathbf{k}_1|y - 4\pi(\nu_{BC2} - \nu_{BC1})t + (\varphi_2 - \varphi_1)]\}. \qquad (27)$$

Equation 27 is the excitation profile described by Eq. 11, where $I_0 = 2|\varepsilon_0|^2$, $k_G = |\mathbf{k}_2 - \mathbf{k}_1|$, $\varphi(t) = \omega_G t + \varphi_G$, $\omega_G = 4\pi(\nu_{BC2} - \nu_{BC1})$, and $\varphi_G = \varphi_2 - \varphi_1$. Thus, the phase of the intensity pattern is swept at the difference frequency $\nu_G = 2(\nu_{BC2} - \nu_{BC1}) = 10$ MHz. Translation of the beam-splitter varies the angle between the beams, thereby adjusting the grating fringe spacing, $d_G = k_G/2\pi$ (17). For the experiments reported below, the range of fringe spacing used is $d_G \sim 1.2–3.5$ μm, corresponding to wave numbers, $k_G = 1.8–5.2$ μm^{-1} The laser power, measured just before sample incidence, is typically set to ~1 μW.

Phase stabilization

An important source of phase noise is ambient room vibrations that ultimately degrade measurement precision. To reduce this noise, we employ

an active-feedback servo in closed-loop configuration to stabilize the phase of the optical grating to <1/100 of the fringe spacing (see Fig. 2, *A* and *B*). Details of the approach, including circuit diagrams, are given by Knowles et al. (19); we include here a cursory description.

The magnified image of the excitation grating at the sample is projected through a Ronche-ruling (Fig. 2 *A*), and subsequently focused onto a small-area avalanche photo-diode (APD; Pacific Silicon Sensor, Westlake Village, CA). As the optical fringe pattern is swept across the ruling, the spatially modulated intensity is converted into a time-varying one. The APD output is measured using a phase-sensitive detector referenced to the difference frequency waveform of the AO-driver ($\nu_G = 10$ MHz). A type 1 servo (19) generates a feedback signal, which is delivered to a Piezoelectric-mounted mirror (model No. STr-25/150/6; Piezomechanik, Munich, Germany), to minimize the relative phase error $RPE \equiv \varphi_{ex} - \varphi_{ref}$ between the excitation and reference waveform phases. In Fig. 2 *B*, we show typical time courses of the *RPE* taken when the fringe spacing is set to $d_G = 1.0 \ \mu$m and the feedback loop is left open (*black curve*) and closed (*red curve*). When the feedback loop is open, passive fluctuations of the *RPE* occur on timescales ranging from 10^{-2}–10^{1} s with root mean-square variation $\langle RPE^2 \rangle^{1/2} \approx 300$ nm, much larger than the scale of motions we wish to detect. When the feedback circuit is closed, the *RPE* continues to fluctuate on the same timescales, but in this case $\langle RPE^2 \rangle^{1/2} \approx 4$ nm. Thus, the precision to which our phase measurements are sensitive is ~(4 nm/d_G) × 360° ≃ 1.4° for $d_G = 1.0 \ \mu$m).

Photon counting phase-synchronous detection

The fluorescence signal (indicated in *red*, Fig. 2 *A*) is collected by the objective, transmitted by the dichroic beam-splitter, and filtered for polarization using an analyzer oriented at the magic-angle (model No. 10FC16PB.3; Newport, Irvine, CA). The fluorescence is spectrally filtered using a 532-nm holographic notch filter (model No. HNPF-532.0-1.0; Kaiser Optical, Ann Arbor, MI), a 650-nm short pass filter (model No. SPF-650-1.0; CVI), and a 700-nm short pass filter (model No. SPF-700-1.0; CVI). The filtered emission is focused onto a low dark-count (<25 Hz) single photon-counting APD (model No. SPCM-AQR-16, 175-μm active area; Perkin-Elmer Optoelectronics, Singapore) using an ultra-long working distance objective lens (model No. SLCPlanFl, 40×, NA 0.55, w.d. 2.6 mm; Olympus, Hauppauge, NY).

In previous FICS experiments, a lock-in amplifier was used to demodulate relatively strong fluorescence signals, which occur when the number of detected photons per modulation period is large (16). As an analog device, the lock-in is designed to process continuous photocurrent signals such as the one depicted in Fig. 3 *A*, thus determining the amplitude $I_0|\hat{O}|$ and phase γ of the modulated waveform. For the experiments presented in this work, the modulated signal is too weak—one photon, on average, for every thirty 10-MHz cycles—to directly process using an analog device. We therefore employ an efficient photon-counting scheme that measures the arrival time of individual photons relative to the reference phase, and assigns to it a bin increment (labeled *j*) that is subsequently stored in digital memory. The process is repeated over an adjustable number of cycles (here 1024), until a statistically relevant histogram (S/N > 250) of intensity versus phase is recorded. A cartoon of a histogram waveform, superimposed with the intensity distribution that it approximates (*dashed curve*), is depicted in Fig. 3 *B*. For the purpose of illustration, a total number of 10 bin increments is shown. However, the actual number of phase increments used in our device is 64, and the mean number of counts per bin is ~30. A detailed description of the time-of-flight histogram generator is given in Appendix B. The completed histogram is converted to analog and output to a lock-in amplifier (model No. 7265 DSP, Signal Recovery, Wokingham, Berkshire, United Kingdom), which is referenced at the carrier frequency $\nu_C = \nu_G/(n \times 64) = 10$ MHz/(16 × 64) = 9.8 kHz with low-pass filter time constant $\tau_{LI} = 5$ ms. The number *n* is adjustable with possible values 1, 2, 4, ..., 32. A computer, which controls an analog-to-digital data acquisition board (National Instruments, Newbury, Berkshire, United
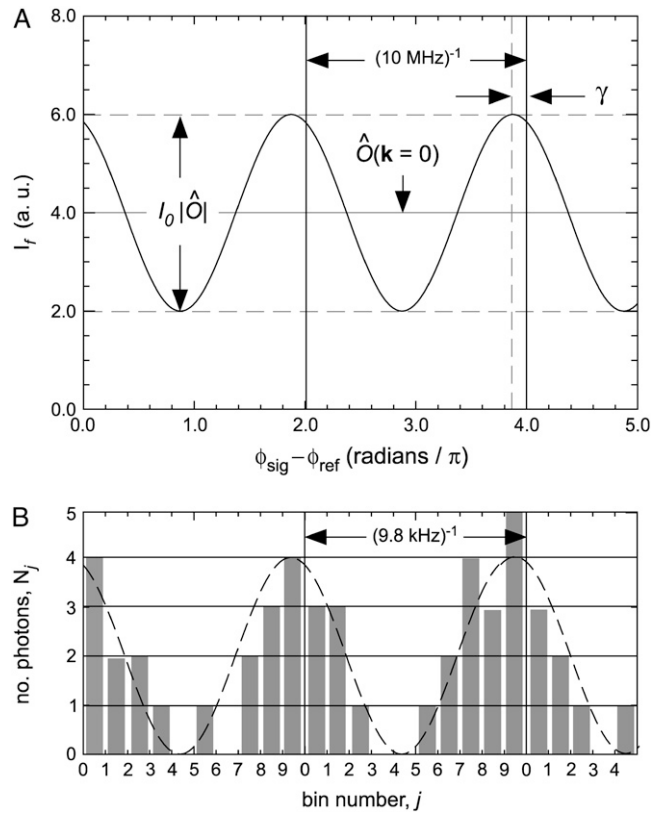

FIGURE 3 (*A*) Schematic of the total fluorescence intensity, $I_f (\phi_{sig} - \phi_{ref})$ (described by Eq. 14), relative to the reference phase. The modulated signal oscillates at the grating sweep frequency, $\nu_G = 10$ MHz, with slowly varying amplitude $I_0|\hat{O}|$ and phase γ. The mean fluorescence background $I_0\hat{O}(0)$ is time-independent. In the strong signal limit (i.e., many detected photons per modulation period), the raw signal is continuous. (*B*) Rough schematic of a phase-dependent intensity histogram resulting from the compilation of $\bar{N}$ independent measurements of single photon arrival times (relative to the reference) (see Appendix B). The phase is divided into *m* bin increments, numbered by the index *j*. (For clarity, $m = 10$ in the figure; the actual value used is $m = 64$.) N_j is the number of photons assigned to bin *j*. The average number of photons per bin shown in the figure is $\bar{N}/m$; 2. The actual value used is $\bar{N}/m \geq 1250 / 64$; 20.

Kingdom), records separately the average fluorescence intensity, $I_0\hat{O}(0)$, the in-phase and in-quadrature components of the demodulated signals, $I_0\text{Re}\hat{O}$ and $I_0\text{Im}\hat{O}$, and the *RPE*. Typically, for each experiment 262,144 successive data points are collected at an acquisition frequency $\nu_{Acq} = 512$ Hz. (For our control colloid measurements, $\nu_{Acq} = 8.2$ kHz.) From these data, the ratio $\frac{1}{\hat{O}(0)}[\text{Re}\hat{O}+i\text{Im}\hat{O}] \propto [\hat{O}]\exp(i\gamma)$ is determined, from which we calculate the function $S(k_G, \tau)$ according to Eq. 16. In practice, the time-correlation functions are computed from the density fluctuation, $\hat{O}(k_G, t)$, by use of the convolution theorem and taking the inverse Fourier transform of the associated power spectral density

$$S(k, \tau) = \frac{1}{\sqrt{2\pi}} \int_{-\infty}^{\infty} d\omega e^{+i\omega\tau} S(k, \omega), \qquad (28a)$$

where

$$S(k, \omega) = \frac{1}{N} \langle \hat{O}^*(k, \omega)\hat{O}(k, \omega) \rangle, \qquad (28b)$$

and

$$\hat{O}(k,\omega) = \frac{1}{\sqrt{2\pi}} \int_{-\infty}^{\infty} d\omega e^{-i\omega\tau} \hat{O}(k,t). \qquad (28c)$$

The normalized time-correlation function $F(k,\tau) = S(k,\tau)/S(k)$ is constructed from Eq. 28a. Individual data sets are repeated $\simeq 10$ times, crosschecked for consistency, and averaged together.

Sample preparation

Stock solutions of wt DsRed were obtained as a gift from Prof. James Remington. The protein concentration of the stock was ~ 20 mg/mL in 50 mM HEPES buffer. One-hundred-and-fifty microliter aliquots of the stock solution were diluted to concentrations ~ 10–50 nM in 95% (by volume) glycerol/water. Samples were prepared by placing 4 μL of solution onto a clean, untreated glass slide and covering with a clean, untreated microscope coverslip. The coverslip was sealed to the slide using UV curing adhesive (Adhesive No. 81, exposure time 3 min; Norland Optical, Cranbury, NJ). The sample itself was masked while the adhesive cured under a long wavelength UV lamp. To address the possibility that the UV treatment might induce covalent cross-links between protein subunits, we analyzed similarly treated samples by gel electrophoresis (10% SDS-PAGE, denaturing). We observed no indication of UV induced cross-linking between protein subunits.

Control measurements, signal/noise, and collection efficiency

In addition to our measurements on DsRed, we present control measurements on dilute (~ 1 nM) aqueous suspensions of polystyrene latex spheres (FluoroSphere, model No. F8801, radius $a = 50$ nm; Invitrogen/Molecular Probes, Eugene, OR). The spheres are uniformly labeled with Rhodamine, which has spectral characteristics similar to those of DsRed. Furthermore, we have adjusted the signal level in our control experiments so that the S/N is comparable to that in our DsRed measurements (see Table 1). For both the latex suspensions and DsRed solutions, blanks with identically prepared solvents were used to determine the background count rate ~ 0.5–1.0 kHz. When the laser was blocked, the signal count rate was the same as the measured dark-count rate ~ 25 Hz.

All samples were positioned at the focal plane of the microscope using a halogen arc lamp to focus on air bubbles trapped between the slide and the coverslip. The temperature of the samples was maintained at $25°C \pm 0.1°C$ using a thermoelectric cooling/heating stage (model No. BC-300W; 20-20 Technologies, Laval, Quebec, Canada) controlled by a closed-loop temperature feedback system (model No. BC-100; 20-20 Technologies). After translation of the stage to a chromophore-rich region, the arc lamp was extinguished and the focus was adjusted to maximize the fluorescence intensity during laser excitation. We verified that this procedure resulted in placing the objective's focus approximately at the midplane of the ~ 10-μm thick sample. Since the objective's depth of field is $<\sim 1$ μm, the signal is derived primarily from particles far from the glass walls of the sample cell.

Typical mean signal count rates $\bar{\nu}_{sig}^{obs}$ for latex and DsRed samples are listed in Table 1. As discussed in M-FICS Instrumentation, the histogram generator constructs an analog ac signal at the carrier frequency $\nu_C = 9.8$ kHz, which is detected as a root-mean square (RMS) voltage using a lock-in

amplifier. The lock-in applies a low-pass filter to the signal with bandwidth ν_{LI} ($= \tau_{LI}^{-1}$, the inverse lock-in time constant). For our measurements on DsRed, $\tau_{LI} = 5$ ms and $\nu_{LI} = 0.2$ kHz; and for the colloid samples, $\tau_{LI} = 640$ μs and $\nu_{LI} = 1.56$ kHz. We estimate the mean number of photons per data point as $\bar{N} = \bar{\nu}_{sig}^{obs}\tau_{LI}$. The S/N associated with these measurements is $\sqrt{\bar{N}(\nu_C/\nu_{LI})}$ (Appendix B), where the factor $\sqrt{\nu_C/\nu_{LI}}$ is the improvement due to the bandwidth of the lock-in amplifier (39) and we have estimated the bandwidth of the input signal by the carrier frequency.

A useful quantity is the mean number of photons detected per data point per molecule, $\bar{N}/N$ (Table 1). For the DsRed samples, $\bar{n} = 10$ nM in the illumination volume $V = \pi(w/2)^2 \Delta z$, with beam diameter $w = 100$ μm and sample thickness Δz; 10 μm. The mean number of molecules in the illumination volume is then $= \langle \delta D_S^2 \rangle / \bar{D}_S^2 \simeq 470,000$. The corresponding number of particles in the latex samples (with $\bar{n} = 1$ nM) is $N \simeq 47,000$. It is clear from the values listed in Table 1 that the S/N ratio can be maintained at an exceptionally high value (>250:1), while the number of photons detected per molecule is small (<0.004).

To determine the instrument collection efficiency, we estimate the emission intensity from the known experimental parameters. Using the extinction coefficient of DsRed ($\varepsilon = 3 \times 10^5$ M^{-1} cm^{-1} for the tetramer) (14), we calculate the absorbance $A = \varepsilon \bar{n} \Delta z = 3 \times 10^{-6}$. The drop in excitation intensity due to transmission through the sample is $\Delta I = I_0[1 - \exp(-A)] \simeq I_0 A = (1 \ \mu W)(3 \times 10^{-6})$, corresponding to $\Delta I = 8.02 \times 10^6$ photons s^{-1}. The expected emission intensity follows from multiplication by the fluorescence quantum yield, $q_F = 0.79$ (14), and the factor $\frac{1}{2}(1 - \cos\sigma_0) = 0.31$ due to the finite collection angle ($2\sigma_0 = 135°$) subtended by the objective lens. This suggests a maximal mean signal count rate of $\bar{\nu}_{sig}^{max} \simeq 2.0$ MHz. We define our collection efficiency as the ratio $\bar{\nu}_{sig}^{obs}/\bar{\nu}_{sig}^{max}$, which lies in the range $1/8$ – $1/5$. These values are reasonable, considering the filtering that occurs before the emission reaches the detector.

In Fig. 4 we plot the normalized ISF, obtained by M-FICS, on the control latex suspensions described above. The decays (shown in *black*) correspond to wave numbers $k_G = 2.09, 2.64, 3.27$, and 3.90 μm^{-1}, and are calculated based on Eq. 28, expressions *a*–*c*. For this dilute fluid system, the decays are expected to follow the Fickian model for self-diffusion of spherical particles given by Eq. 8. Indeed, we find that the time and wave-number dependences of the correlation functions are in excellent agreement with Eq. 8 (shown as *gray dashed curves*) with self-diffusion coefficient $D_S = 4.3$ μm^2 s^{-1}. This value for D_S is in excellent agreement with the free diffusion coefficient calculated from the Stokes-Einstein equation, where we have used the viscosity of water $\eta = 1$ cP and the hydrodynamic radius $a = 50$ nm. We note that for each of the wave numbers investigated, the decays are well described as single-exponential out to two decades below the initial amplitudes. These measurements serve as a control diagnostic to test the working order of the M-FICS instrument under S/N conditions similar to those used for our fluorescent protein measurements.

RESULTS AND DISCUSSION

According to Eqs. 17 and 24, when the fluorescence signal is selected for polarization at the magic-angle, the ISF computed from our data takes the form

$$S(k,\tau) \approx (\kappa'_{MA})^2 F_S(k,\tau) \propto F_S(k,\tau). \qquad (29)$$

TABLE 1 Sample signal characteristics

Sample	ν_{Acq}/kHz	$\bar{\nu}_{sig}^{obs}$/kHz	$\bar{N}$	S/N	$\bar{N}/N$
0.1 μm colloid	8.2	800–1200	512–768	56–69	0.011–0.016
DsRed	0.512	250–400	1250–2000	247–313	0.003–0.004

The value ν_{Acq} is the data acquisition frequency; $\bar{\nu}_{sig}^{obs}$ is the observed signal count rate; $\bar{N}$ is the mean number of photons per integrated histogram; S/N $= \sqrt{\bar{N}(\nu_C/\nu_{LI})}$ is the signal/noise ratio of a single measurement with $\nu_C = 9.8$ kHz; $\nu_{LI} = 0.2$ kHz; and $\bar{N}/N$ is the mean number of photons detected per particle in a single measurement. See discussion in Control Measurements, Signal/Noise, and Collection Efficiency.
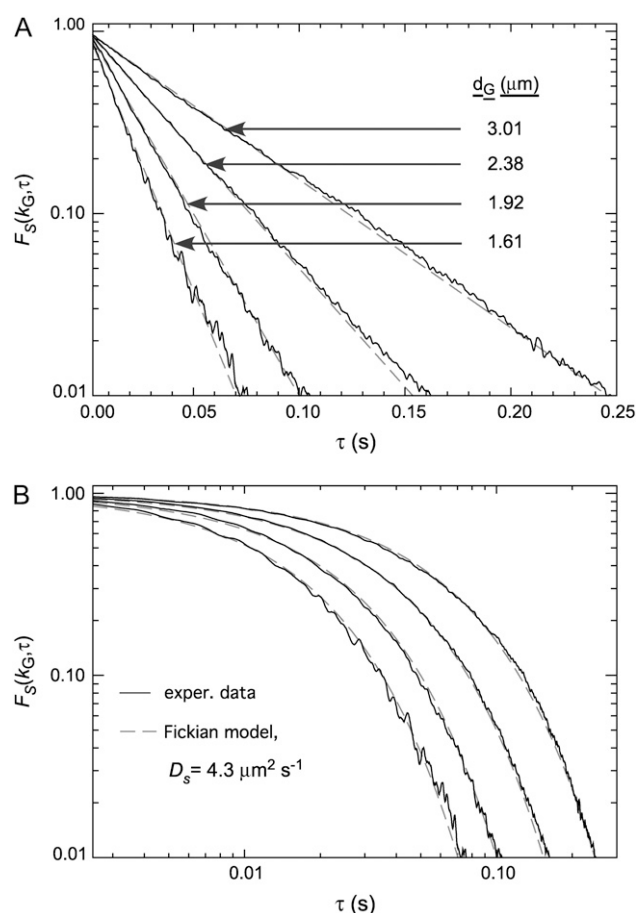
FIGURE 4 Normalized self-ISF $F_S(k,\tau)$ determined by M-FICS on 0.1-μm diameter Rhodamine-labeled poly(styrene) beads in aqueous suspension. The ISF is shown for wave numbers $k_G = 2\pi/d_G = 2.09$, 2.64, 3.27, and 3.90 μm^{-1}. (Values for the fringe spacings d_G are given in the figure.) Dashed blue curves are plots of the Fickian model (Eq. 8) with $D_S = 4.3$ μm^2 s^{-1}. Data and models are shown on log-linear (A) and log-log (B) scales.

In Eq. 29, the constant $(\kappa'_{MA})^2 = (\kappa_{MA})^2[1 - 0.1826\bar{P}_2]$. We therefore expect the detected signal to be independent of optical anisotropy transients, and to only reflect translational motions. Nevertheless, it is possible for the molecules to undergo a photoconversion process on measurement timescales, such as photodegradation, spectral diffusion, or inter-system crossing between bright and long-lived dark states (often called flickering) (22). In this hypothetical situation, the fluorescence-detected excited state population would fluctuate due to the photoconversion process. Because the rates of such processes depend on laser excitation intensity, we would expect their presence to be revealed as intensity-dependent contributions to the decay of the ISF.

Previous studies of DsRed and fluorescent protein mutants, both at the single-molecule level (20) and using conventional fluorescence correlation spectroscopy (21,22,40), have reported photoinduced transitions occurring on sub-millisecond timescales. In those studies, the range of excitation intensities

examined is 0.4–100 kW cm^{-2}. For comparison, the maximum excitation intensity used in our experiments is ~1 μW/$\pi(50 \ \mu$m$)^2 = 1.3 \times 10^{-5}$ kW cm^{-2}, which is ~30,000–8,000,000 times smaller than those used in the photoconversion studies (20–22,40). The relatively small excitation intensity used in our experiments is possible because of the significant number of molecules inside the illumination volume ($N \simeq 470{,}000$), which is nevertheless small enough to generate a fluctuating M-FICS signal proportional to number density fluctuations.

In Fig. 5, we show the ISF obtained from M-FICS experiments on dilute DsRed solutions, and as a function of the laser excitation intensity. The ISF is measured at the wave numbers $k_G = 2.45$, 2.96, and 3.59 μm^{-1}, and is shown on a vertical scale encompassing one factor of e. For each wave number, we show superimposing decays corresponding to three different laser intensities: $I_0 = 1.27 \times 10^{-5}$ kW cm^{-2} (black), 0.16×10^{-5} kW cm^{-2} (gray), and 0.04×10^{-5} kW cm^{-2} (white). Our results indicate that the functional form of the ISF is independent of excitation intensity, although the S/N ratio degrades significantly with decreasing intensity (e.g., S/N $\sim$ 43:1–55:1 for the lowest intensity value). Indeed, for all of our measurements, which are conducted under similar conditions, the ISF (with time resolution ≥ 5 ms) does not exhibit a dependence on excitation intensity. This suggests two possible explanations: 1), The photoinduced dynamics associated with the DsRed system occur on timescales outside of the measurement bandwidth (200–0.01 Hz); or 2), for the low excitation intensities used in our experiments, the steady-state fraction of DsRed molecules populating nonradiative (dark) states is negligibly small. Several workers have associated the photoinduced dynamics observed in fluorescent proteins
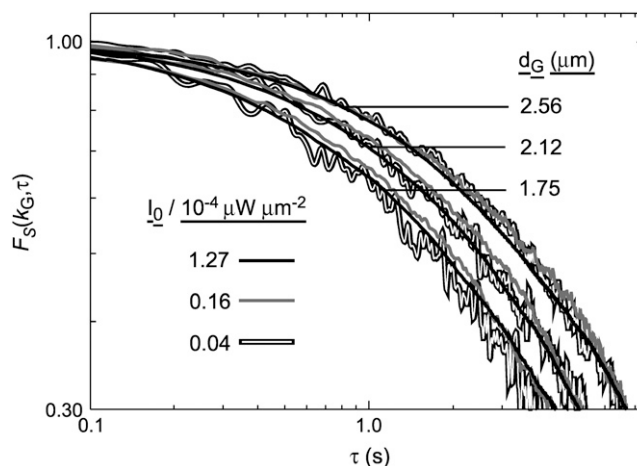

FIGURE 5 Normalized self-ISF $F_S(k,\tau)$ determined by M-FICS on dilute solutions of DsRed in 95% (by volume) glycerol/water. The different decays correspond to wave numbers $k_G = 2\pi/d_G = 2.45$, 2.96, and 3.59 μm^{-1}. (Values for the fringe spacings d_G are given in the figure.) For each wave number, measurements are superimposed corresponding to excitation intensities, $I_0 = 1.27$ (black), 0.16 (gray), and 0.04 (white) $\times 10^{-4}$ μ W μm^{-2} ($\times$ 10^{-5} kW cm^{-2}).

with slow conformational changes in molecular structure (21,22,41–45). If this mechanism is correct, our observations could support the notion that conformational fluctuations linked to photoconversion processes occur on faster time-scales than those sampled in our current measurements.

Having established that our measurements probe the translational self-displacements of DsRed molecules, we now turn to studies of DsRed diffusion. In Fig. 6 we show measurements of the ISF for dilute DsRed solutions, corresponding to wave numbers $k_G = 2.15$, 2.45, 2.96, 3.59, 4.49, and 5.46 μm^{-1} (shown in *black*). These data are plotted on log-linear (Fig. 6 A) and log-log (Fig. 6 B) scales. For each wave number, comparison is made to the Fickian model for the self-ISF (Eq. 8) (shown as *dashed white curves*), and the second-order cumulant approximation (Eq. 10) (shown as *dashed gray curves*). We first discuss the relationship to the Fickian model. At relatively short times (subsecond scales),
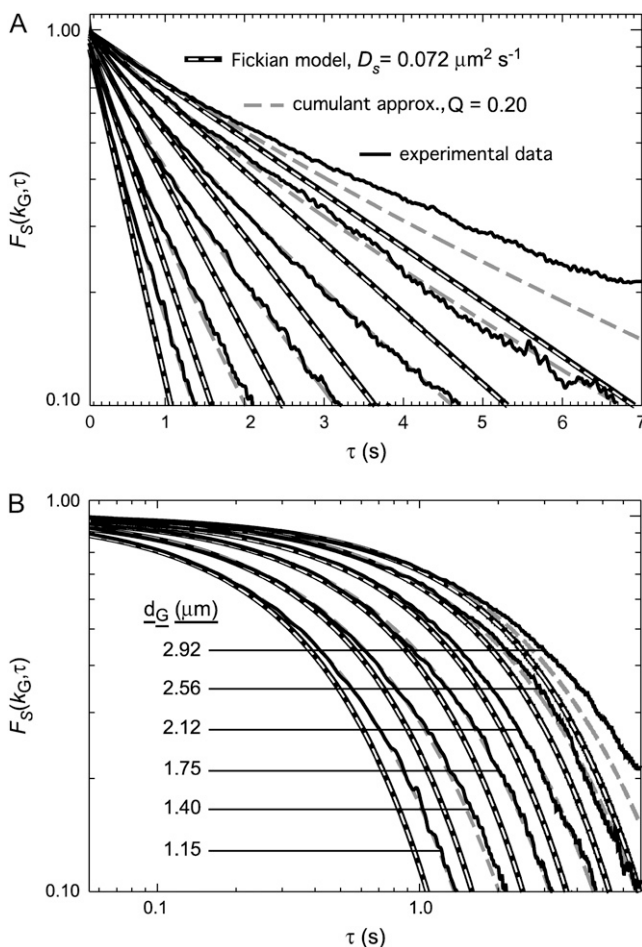

FIGURE 6 Normalized self-ISF determined by M-FICS on DsRed in 95% (by volume) glycerol/water solution. The different decays correspond to wave numbers $k_G = 2\pi/d_G = 2.15$, 2.45, 2.96, 3.59, 4.49, and 5.46 μm^{-1}. (Values for the fringe spacings d_G are given in the figure.) Dashed white curves are plots of Eq. 8 with $D_S = 0.072$ $\mu m^2 s^{-1}$. Dashed gray curves are plots of Eq. 10 with $D_S = 0.072$ $\mu m^2 s^{-1}$ and $Q = 0.20$. Data and models are shown on log-linear (A) and log-log (B) scales.

all of the decays appear as single-exponentials and are well described by the Fickian model with self-diffusion coefficient $D_s = 0.072$ $\mu m^2 s^{-1}$. We wish to compare our measured value for D_s to that predicted by the Stokes-Einstein equation, based on consideration of the crystallographic data for DsRed (13). If we take into account the known tetrameric structure of the DsRed molecule, its hydrodynamic properties can be reasonably modeled assuming an oblate ellipsoidal shape with semi-major axis of length 4.4 nm, semi-minor axis of length 2.2 nm, and axial ratio $p_r = 2$ (46). The value for the self-diffusion coefficient predicted by the Stokes-Einstein equation is then $D_S = k_B T/f = 0.077$ $\mu m^2 s^{-1}$, where $f = 6\pi\eta r_{sph}F$ is the hydrodynamic drag coefficient, η ($= 779$ cP) is the viscosity of the 95% (by volume) glycerol-water solvent (47), r_{sph} ($= 3.49$ nm) is the radius of a spherical particle with equal volume to that of the ellipsoid, and F ($= 1.042$) is the Perrin shape factor (46). Our measured value for D_s is within 6% of the Stokes-Einstein prediction based on the expected viscosity of the solution. If we assume that the measured value for D_s is correct and calculate the viscosity, we obtain $\eta = 837$ cP, which corresponds to a glycerol-water composition of 95.4% (47). This discrepancy between our measured value for D_s and the Stokes-Einstein prediction could be, in principle, due to a small error in the composition of our glycerol/water solution. Nevertheless, because of the close agreement between the measured and predicted values of D_s, we conclude that the short-time behavior of the ISF is dominated by the self-diffusion of the tetrameric DsRed species.

On timescales >1 s, the functional form of the ISF departs from single exponential behavior. For all of the wave numbers investigated, the decays are generally slower than the Fickian prediction. As discussed in Theoretical Background, deviations from Fickian behavior can be explained in terms of observing a distribution of local molecular mobilities. Our primary concern here is to establish our ability to identify and characterize such a distribution. The physical origin of the distribution is a secondary question, which we address by discussing two possible explanations. For example, if the DsRed molecules were to undergo a chemical reaction to form higher-order oligomeric species, we would expect the observed ISF to reflect the underlying distribution of species-dependent self-diffusion coefficients. On the other hand, molecular diffusion of identical molecules through a dynamically heterogeneous solvent can also lead to observations of a distribution of mobilities. In this case, the local environments experienced by different molecules are different because of anomalous properties of the host solvent. We discuss these scenarios further below.

To account for the stretched-exponential behavior in the ISF (Fig. 6), we adopt the second-order cumulant approximation given by Eq. 10. The second-order term is proportional to the parameter $Q = \{[\langle D_S^2 \rangle/\bar{D}_S^2] - 1\} = \langle \delta D_S^2 \rangle/\bar{D}_S^2$, which is a measure of the variance $\langle \delta D_S^2 \rangle$ of the distribution of molecular diffusivities. In Fig. 6, we show plots of Eq. 10 (*green curves*) where we have set the mean value of the

distribution $\bar{D}_S = 0.072$ μm^2 s^{-1} (consistent with the observed short-time Fickian behavior) and $Q = 0.2$. We note that, with the exception of the $k_G = 2.15$ μm^{-1} dataset, the cumulant approximation perfectly matches all of our data out to relatively long timescales. We obtain from this fit a standard deviation $\langle \delta D_S^2 \rangle^{1/2} = 0.032$ μm^2 s^{-1}. These values for $\bar{D}_S$ and Q correspond to the best fits of Eq. 10 to our data. We note that our confidence in the fit is bolstered by the fact that our determination of the ISF includes independent measurements over six different values of k_G. As in all Fourier-space measurements, the redundancy of dynamical information contained by the set of k_G-dependent experiments is an important strength of the M-FICS approach. A favorable comparison between experimental data and theoretical models is supported by self-consistency over the full range of spatial and temporal scales accessed by the measurement. The excellent agreement between our data and Eq. 10 for the first five of six measured length scales strongly suggests that, at least for these scales, there is a distribution of diffusivities with characteristic width determined by Q. The apparent disagreement between the $d_G = 2.92$ μm data set and Eq. 10 is most likely due to a qualitative change in the properties of the distribution for length scales >2.56 μm.

We now turn to the question of the physical origin of the distribution characterized by our data. As mentioned previously, one possibility is that higher-order noncovalent aggregates of DsRed form at equilibrium, so that our observations reflect the collective dynamics of a mixture of oligomeric species. If the system under study were composed of a discreet distribution of species, we would expect the ISF to be a weighted average over the individual species contributions,

$$F_S(k, \tau) = \sum_j B_j e^{-k^2 D_j \tau} / \sum_j B_j, \qquad (30)$$

where B_j is the spectral amplitude of species j, and D_j is the self-diffusion coefficient. For purposes of illustration, we consider the effect of the simplest nontrivial distribution. Phillies (48) has recently discussed the light scattering spectrum of a bi-disperse system, in which case

$$F_S(k, \tau) = \frac{B_1 e^{-k^2 D_1 \tau} + B_2 e^{-k^2 D_2 \tau}}{B_1 + B_2}. \qquad (31)$$

We apply the method of cumulants (25,48) to this distribution to obtain the relationships

$$\bar{D}_S = \frac{B_1 D_1 + B_2 D_2}{B_1 + B_2} \quad \text{and} \quad Q = B_1 B_2 \left[\frac{D_1 - D_2}{B_1 D_1 + B_2 D_2} \right]^2. \qquad (32)$$

We now reconsider the second-order cumulant approximation

$$F_S(k^2 \bar{D}_S \tau) = e^{-(k^2 \bar{D}_S \tau)} \left\{ 1 + \frac{1}{2} Q(k^2 \bar{D}_S \tau)^2 \right\}, \qquad (33)$$

where we have written the function in terms of the combined space-time variable $k^2 \bar{D}_S \tau$. Equation 33 shows that a plot of

the self-ISF versus $k^2 \bar{D}_S \tau$ is independent of k_G, and that all of the properties of the system are contained in the parameters $\bar{D}_S = 0.072$ μm^2 s^{-1} and $Q = 0.2$. We see that the leading term of the ISF, which dominates its short-time behavior, is determined by the mean value of the diffusion coefficient $\bar{D}_S$. According to the Eq. 32, we can interpret $\bar{D}_S$ as a collective diffusion coefficient. On very long timescales, the second-order term in Eq. 33 becomes dominant. According to Eq. 32, this second-order term is proportional to the relative diffusion of the two species. For intermediate timescales, the ISF exhibits a crossover from the short-time dynamics associated with collective motions to the long-time dynamics indicative of relative motions.

To compare our results to the predictions of a bi-disperse distribution, we require a simple model for the two species under consideration. Since our data successfully describe the free diffusion of the DsRed tetramer at short times, it is reasonable to assume the tetramer as one of the two diffusing species (labeled 1). If we also assume that our preparation of the solvent composition is accurate, we may use the predicted Stokes-Einstein value for the diffusion coefficient, $D_1 = 0.077$ μm^2 s^{-1}. A reasonable guess for the structure of the aggregate species is an octomer in which the planar cross-sections of two DsRed tetramers form the opposing faces of a cube with the diagonal length of the cube face equal to 8.8 nm. We estimate the diffusion coefficient of this species by assuming a spherical shape with hydrodynamic radius equal to one-half the length of the cube diagonal, i.e., $a = 5.39$ nm. This model leads to a Stokes-Einstein value for the octomer diffusion coefficient $D_2 = 0.052$ μm^2 s^{-1}. The constraints given by Eq. 32 and the normalization condition, $1 = B_1 + B_2$, form a system of overdetermined equations in the unknown spectral amplitudes B_1 and B_2. Based on the values for $\bar{D}_S$ and Q obtained from our fit, and those for D_1 and D_2 proposed from our model, we obtain $B_1 = 0.8$ and $B_2 = 0.2$.

In Fig. 7, we plot the ISF versus $k^2 \bar{D}_S \tau$ for the $k_G = 2.45$, 2.96, 3.59, 4.49, and 5.46 μm^{-1} data that were shown in Fig. 6. As expected, all five data sets collapse onto a universal curve described by Eq. 33 (shown in *gray*). Also in Fig. 7, we plot model Fickian decays corresponding to the free diffusion of the DsRed tetramer with diffusion coefficient D_1 (*solid black curve*) and the model octomer with diffusion coefficient D_2 (*dashed black curve*). Both the cumulant and our data show a time-dependent crossover from the dynamics characteristic of the tetramer to those of the octomer. We conclude that our data are consistent with this model based on an equilibrium distribution of 80% tetramer and 20% octomer.

A second possible explanation for our observations of dispersion in the DsRed mobility is that the medium itself is dynamically heterogeneous (27,49,50). It is well known that as a fluid approaches its glass transition temperature, the behavior of dynamic processes such as molecular rotation and translation become complex. Nonexponential relaxations are the signature of disordered systems, which often give rise to anomalous tracer particle diffusion (51). Since our experiments
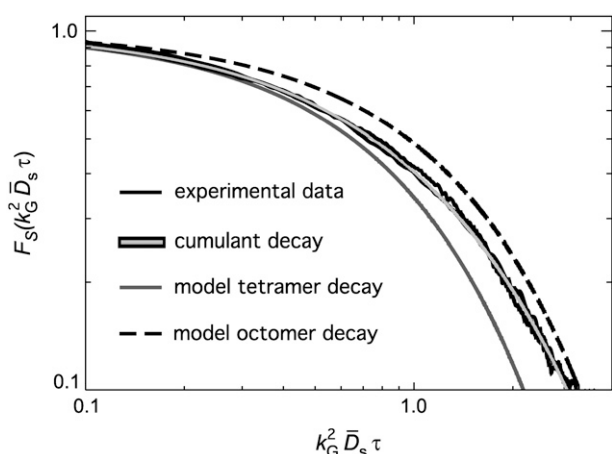
FIGURE 7 Normalized self-ISF (same data as Fig. 6) plotted versus $k_G^2 \bar{D}_S \tau$ (Eq. 33) with $\bar{D}_S = 0.072 \ \mu m^2 \ s^{-1}$. The experimental data correspond to wave numbers $k_G = 2\pi/d_G = 2.45, 2.96, 3.59, 4.49,$ and $5.46 \ \mu m^2 \ s^{-1}$. Also shown are plots of Eq. 33 with $\bar{D}_S = 0.072 \ \mu m^2 \ s^{-1}$ and $Q = 0.2$. (*gray curve*), and two model Fickian decays corresponding to a DsRed tetramer (*solid black curve*) and a DsRed octomer (*dashed black curve*).

are conducted in viscous 95% glycerol/water, it is possible that proximity to the glass transition temperature is related to the nonexponential features we observe in the ISF. However, the glass transition temperature of glycerol is >100° below room temperature ($T_g \approx 190$ K), so that we might expect the effects of dynamic disorder to be negligible. With this in mind, we look to dielectric impedance measurements of glycerol/water mixtures (52,53). Frequency-domain impedance analysis is a method frequently applied to study the distribution of relaxation times in glass-forming liquids. Measurements of the dielectric loss spectrum determine if the relaxation time distribution is broadened with respect to single-exponential (Debye) behavior. Feldman and co-workers have recently reported dielectric relaxation measurements for 90% glycerol/water mixtures near room temperature (52). These studies indicate that high glycerol content mixtures behave similarly to pure glycerol at room temperature, and that the distribution of solvent molecular relaxation times is indeed asymmetrically broadened. The broadened dielectric loss spectrum is peaked at ~1 GHz. It is further quantified by the Cole-Davidson parameter, $\beta_{CD} \simeq 0.67$, and can be expressed as the ratio $W/W_D \simeq (1.19)$ of the measured spectral width W to that expected for a single-exponential Debye process (W_D, encompassing 1.14 decades). Curiously, the above value for W/W_D is consistent with our determination of the parameter $Q+1 = 1.2 = \langle D_S^2 \rangle / \bar{D}_S^2$. Were our M-FICS experiments designed to directly probe the host solvent self-diffusion on nanosecond timescales, we might expect to observe anomalous behavior similar to that revealed by the dielectric loss spectrum. Nevertheless, our experiments probe the self-diffusion of relatively large DsRed protein molecules that are several times the size of the solvent molecules (<1 nm). Furthermore, our measurements sample the protein displace-

ments on timescales that are many times the mean relaxation time of the solvent molecules (~1 ns). In fact, our experimental conditions should correspond to the so-called hydrodynamic limit of liquid state theory (54), for which DsRed self-diffusion is expected to follow simple Fickian behavior.

Based on the above reasoning, it appears that our observations cannot be explained by the sole effects of dynamic disorder in the 95% glycerol/water medium. We conclude that the presence of a bi-disperse distribution is the more likely explanation. Further investigation is necessary to confirm the bi-disperse distribution hypotheses.

CONCLUSIONS

We have demonstrated a new experimental approach, called molecular Fourier imaging correlation spectroscopy (M-FICS), to sample the distribution of the center-of-mass fluctuations of fluorescent molecules in viscous solution. Under the appropriate conditions (i.e., low excitation intensity ~1.27×10^{-5} kW cm^{-2}, 5 ms integration time, magic-angle detection) we may avoid detection of photoconversion phenomena and isolate signal contributions due solely to translational motions. The signal/noise is sufficiently high (S/N $\geq$ 250:1) to extract information about the underlying distribution of the local molecular mobility. M-FICS can therefore provide similar and complementary information to that obtained from single-molecule spectroscopic experiments. The high S/N ratio is maintained while minimizing the number of photons detected per molecule, thus reducing the effects of photodegradation and photoinduced flickering. The M-FICS approach efficiently samples statistical ensembles, since the total number of successive measurements scales with N ($\approx$500,000)—the average number of molecules inside the illumination volume.

For these initial studies, we have focused on DsRed for its high extinction coefficient and fluorescence quantum yield. By increasing the excitation intensity, the signal level and S/N can be improved. Future applications of the M-FICS technique will include measurements on faster timescales (~1 μs), and on various chromophore systems including monomeric fluorescent proteins. As a Fourier-space fluctuation spectroscopy, M-FICS is best applied to samples containing low concentrations of fluorophores. The signal fluctuations arise from different configurations of molecules as they project onto the intensity fringe pattern with spacing d_G. Since the diffraction limit for visible light microscopy requires the minimum value of d_G to be in the range $\lambda_{ex}/2 \simeq 0.2$–0.5 μm, the concentration levels most suitable to M-FICS are in the range 1–50 nM. In the current studies we have accurately determined diffusion coefficients over the range 0.07–4 μm^2 s^{-1}. With further technical improvements, we expect to increase the accessible dynamic range by four decades toward faster timescales.

Techniques such as dynamic light scattering and ultracentrifugation are traditional methods to study the hydrodynamic

properties of biomolecular species. However, the former is a relatively low S/N technique, while the latter is an invasive method. Because M-FICS detects signal fluctuations from fluorescent species, the potential exists to perform these measurements with high S/N and molecular sensitivity in intracellular compartments. One can envision live cell applications using the M-FICS technique. M-FICS studies performed on selectively labeled proteins in the cell could provide information about the dispersion of target sites associated with that species. Protein aggregation, protein-protein interactions, and filament polymerization and depolymerization could potentially be investigated. Because the cell interior is thought to be a highly viscous and crowded environment (3,4), the relatively high viscosities investigated in the current work are a reasonable starting point for live cell studies.

M-FICS measurements that select for polarization can, in principle, be used to separate molecular orientational degrees of freedom from center-of-mass motions. We have discussed the significance of the dipole relaxation time correlation function, $\langle \bar{P}_2(t) \bar{P}_2(t+\tau) \rangle$, and its role on the M-FICS signal. In our current studies, the effects of anisotropy fluctuations were intentionally minimized. Nevertheless, future measurements at low temperatures approaching the glass transition will have the ability to separately determine the distributions of molecular orientational and translational motions. Furthermore, polarization-resolved experiments on macromolecular complexes containing (naturally or through engineering) optically coupled electronic transition dipoles, could reveal detailed information about slow conformational fluctuations. Finally, a polarization-resolved M-FICS approach could be used to monitor pairwise molecular interactions, since the dipole relaxation function $\bar{P}_2$ is expected to fluctuate as pairs of molecules diffuse within the range of intermolecular dipolar coupling.

APPENDIX A

The intensity of a single molecular dipole, observed with high numerical aperture and magic-angle polarization

To calculate the high numerical aperture (NA) magic-angle intensities from individual molecular dipoles, it is necessary to account for the dipole's orientation with respect to a laboratory fixed coordinate system. Three aspects of the experimental apparatus are specified by the laboratory frame; the optic axis of the microscope, the polarization vector of the excitation laser, and the orientation of the analyzer that determines the polarization of the detected fluorescence. We follow the procedure outlined by Axelrod to determine the high NA intensities with parallel and perpendicular polarizations in the laboratory frame (36,37).
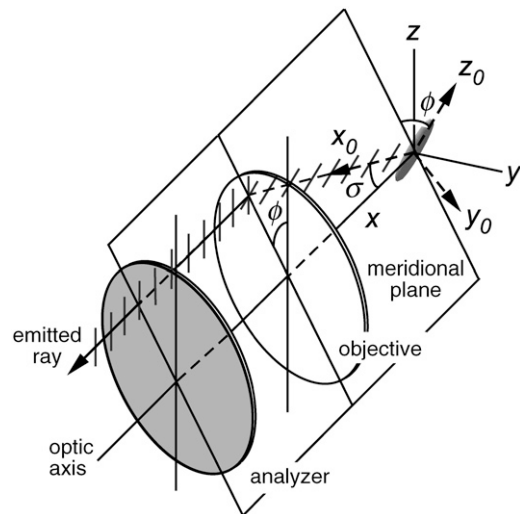
FIGURE 8 Ray diagram for high numerical-aperture polarization-selective detection (described in Appendix A). A single molecular dipole (*shaded gray*) resides at the origin of the object frame, and emits a ray in the direction of the objective lens. The objective acts to refract the ray, changing its propagation vector from x_0 (in the object frame) to x (in the laboratory frame), and its polarization vector from z_0 to z. The angle ϕ between the polarization vector and the meridional plane (the plane containing the optic axis and the ray propagation vector) is the same in both the object and laboratory frames.

A molecular dipole is situated at the origin of a right-handed coordinate system with axes, x_0, y_0, z_0, designated the object frame (Fig. 8). The object frame shares a common origin with the laboratory coordinate system, which has axes x,y,z. The dipole (shown as a *gray ellipsoid*) emits a fluorescent ray that propagates parallel to the x_0 axis with plane polarization (indicated with *gray line segments*) parallel to the z_0 axis. The ray is refracted by an objective lens, which acts to rotate the propagation vector parallel to the optic axis of the microscope (the x axis), and the polarization vector parallel to the laboratory fixed z axis. (An analyzer is placed in the path subsequent to the objective to select z-polarization.) The relative orientation of the two frames is specified by the polar angle σ, which subtends the x_0- and x axes, and the azimuthal angle ϕ, which subtends the z axis and the meridional plane. The meridional plane is defined such that it contains the optic axis and the ray propagation vector. It is important to note that the angle ϕ, between the polarization vector and the meridional plane, is the same in both the object and laboratory frames. Thus, rays selected by the analyzer oriented vertically in the laboratory frame (polarized along the z axis) are necessarily polarized along the z_0 axis in the object frame. An analogous argument can be made for rays selected by a horizontally oriented analyzer, in which case the polarization must be parallel to the y_0 axis in the object frame. Similarly, rays that are selected by orienting the analyzer at an arbitrary angle, θ_{det} with respect to the z axis, will have polarization along the direction $\cos\theta_{det}z_0 + \sin\theta_{det}y_0$ in the object frame.

The coordinates of the dipole in the object frame can be related to those in the laboratory frame through the rotation transformation,

$$\begin{pmatrix} x_0 \\ y_0 \\ z_0 \end{pmatrix} = \begin{pmatrix} \cos\sigma & \sin\sigma\sin\phi & -\sin\sigma\cos\phi \\ -\sin\sigma\sin\phi & \cos\sigma\sin^2\phi + \cos^2\phi & -\cos\sigma\sin\phi\cos\phi + \sin\phi\cos\phi \\ \sin\sigma\cos\phi & -\cos\sigma\sin\phi\cos\phi + \sin\phi\cos\phi & \cos\sigma\cos^2\phi + \sin^2\phi \end{pmatrix} \begin{pmatrix} x \\ y \\ z \end{pmatrix}. \tag{A1}$$

Operationally, the matrix performs three successive rotations: 1), a rotation of ϕ about the x axis; 2), a rotation of $-\sigma$ about the new y axis; and 3), a rotation of $-\phi$ about the newest x axis. The integrated intensity associated with all rays emitted by the dipole for arbitrary analyzer orientation is given by

$$I_{\theta_{\text{det}}} = \int_{\sigma=0}^{\sigma_0} \sin\sigma d\sigma \int_{\phi=0}^{2\pi} d\phi (\cos\theta_{\text{det}} z_0 + \sin\theta_{\text{det}} y_0)^2. \quad \text{(A2)}$$

The integrand of the second nested integral in Eq. A2 is equal to $\cos^2 \theta_{\text{det}}$ $(z_0)^2 + \sin^2 \theta_{\text{det}} (y_0)^2 + 2\cos \theta_{\text{det}} \sin\theta_{\text{det}} (y_0 \cdot z_0)$. Since the cross-term is proportional to the dot product between the two orthogonal vectors (y_0 and z_0), only the self-terms remain. Equation A2 therefore simplifies to

$$I_{\theta_{\text{det}}} = \cos^2\theta_{\text{det}}I_{\parallel} + \sin^2\theta_{\text{det}}I_{\perp}, \quad \text{(A3)}$$

where $I_{\parallel}$ and $I_{\perp}$ represent the observed high numerical aperture intensities if the analyzer is oriented with $\theta_{\text{det}} = 0°$ and $\theta_{\text{det}} = 90°$, respectively. Since we are interested in measurements with the analyzer orientated at the magic-angle ($\theta_{\text{det}} = 54.736°$), we substitute this value into Eq. A3 to obtain $I_{\text{MA}} = \frac{1}{3} I_{\parallel} + \frac{2}{3} I_{\perp}$ or $I_{\text{MA}} \propto I_{\parallel} + 2I_{\perp}$.

Carrying out the integration in Eq. A2 leads to (36,37)

$$I_{\perp} = K_a I_x + K_c I_y + K_b I_z, \quad \text{(A4a)}$$

and

$$I_{\parallel} = K_a I_x + K_b I_y + K_c I_z, \quad \text{(A4b)}$$

where the NA-dependent constants K_a, K_b, and K_c are given by the expressions in Eq. 19, a–c. In Eqs. A4a and A4b, we have made the assignments, $I_x = |x|^2$, $I_y = |y|^2$, and $I_z = |z|^2$, which are the laboratory frame intensities that would be observed in the low NA limit. The relationship between the low-NA intensities and the fluorescence anisotropy is well known (25,38):

$$I_x = 1 - \frac{2}{5}\bar{P}_2, \ I_y = 1 - \frac{2}{5}\bar{P}_2, \ I_z = 1 + \frac{4}{5}\bar{P}_2. \quad \text{(A5)}$$

Substitution of Eq. A5 into the expressions in Eq. A4 and making use of the expression $I_{\text{MA}} \propto I_{\parallel} + 2I_{\perp}$ leads to

$$I_{\text{MA}} \propto \left\{ (K_a + K_b + K_c) + \frac{2}{5}\bar{P}_2(K_b - K_a) \right\}, \quad \text{(A6)}$$

which is the same expression used for the molecular intensity given by Eq. 18.

APPENDIX B

Single photon counting phase-sensitive detection

An essential step in M-FICS experiments is to measure the distribution of fluorescence intensity as a function of the phase of the spatially modulated excitation (given by Eq. 14). In the current studies, the signal count rate is within the range $\bar{\nu}_{\text{sig}}^{\text{obs}} = 250$–$400$ kHz (see Table 1) and the grating modulation frequency $\nu_G = 10$ MHz. Consequently, only one photon is detected (on average) for every 25–40 fringe cycles (2.5–4 μs), a timescale much greater than the chromophore lifetime ($\tau_F \sim 3.5$ ns) (33). In this low signal limit, it is advantageous to use photon-counting detectors that efficiently discriminate against electronic shot noise (<25 Hz). We are then faced with the task of assigning a phase to each detected photon, and to record and repeat the operation until the desired phase-dependent intensity distribution has been obtained. The overall procedure is continuously reiterated at the lock-in carrier frequency.

Fig. 9 illustrates the electronics used to construct histograms of photon phase relative to the excitation (see Figs. 1 and 2). In Fig. 9 A, we show a rough schematic diagram of our time-of-flight histogram generator. The composition of the circuit involves three successive stages:

1. a digital sample and hold constructed with a 6-bit counter and latch;
2. an array generator that employs multiple memory addresses and allows for continuous input/output data streaming; and
3. a digital-to-analog converter that outputs a continuous waveform.

The counter is triggered by the 10-MHz reference discussed in the text. A phase-locked loop is established between the reference and a 640-MHz clock, which generates a 6-bit saw-tooth waveform (64 incremental values) that is synchronously reset at the reference frequency. The counter output (depicted in Fig. 9 B) is relayed via a six-bit data bus to a latch, which functions to retain the value of the counter coincident with a signal detection event. Fig. 9 C depicts a hypothetical sequence of three TTL signal events, with countervalues a, b, and c, respectively. The counter values are each in turn converted to a six-bit number representative of the phase (as depicted in Fig. 9 D), and subsequently output to digital memory. The memory stores and retains counter values, partitioned into 64 possible bin increments (Fig. 9 E). The histogram is built up over an adjustable number of 10 MHz cycles ($n \times 64$, where $n = 1, 2, 4, \ldots, 32$), at which point it is output to the digital-to-analog converter at the carrier frequency $\nu_C = 10$ MHz/($n \times 64$). In our current experiments, $n = 16$, and $\nu_C = 9.8$ kHz. To avoid unnecessary dead-time effects, we employ a toggle flip-flop (not shown) to sequentially alternate between histogram storage and readout at two separate memory locations. The flip-flop is synchronously toggled at the frequency ν_C.

Signal/noise analysis

Perhaps the greatest potential source of noise in our detection scheme is possible differential nonlinearity (DNL) associated with the digital counter and latch. This would lead to systematic errors in the assignments of phase bins to photon arrival times, and would bias our phase measurements. In principle, the effects of DNL can be removed by instrument calibration. For the current studies, we observed no bias in control colloid experiments (e.g., Fig. 4) to indicate that correction for DNL is necessary.

To evaluate the signal/noise associated with a given measurement, we consider an intensity histogram such as the one depicted in Fig. 3 B. The full range of possible phase angles is divided into $m = 64$ bin increments, numbered by the index $j (= 0, 1, \ldots, 63)$. We define $\bar{N}$ as the total number photons detected during the integration period, and N_j the number of photons stored in bin increment j, such that $\sum_{j=0}^{m-1} N_j = \bar{N}$. For the experiments presented here, the average number of photons per bin is $\bar{N}/m \geq 1250/64 \simeq 20$. The probability p_j that any one randomly sampled measurement will result in an assignment to bin j is given by

$$p_j = \frac{I_f(\phi_j)\Delta\phi}{\sum_{j=0}^{m-1} I_f(\phi_j)\Delta\phi}, \quad \text{(B1)}$$

where $\Delta\phi = 2\pi/m$, $\phi_j = j\Delta\phi$, and $I_f(\phi_f) = I_0\{\hat{F}(0) + |\hat{F}|\cos(\phi_j + \gamma)\}$ (see Eq. 14). We wish to know the accuracy of the probability distribution function, $P_j(N_j)$, of obtaining N_j of the $\bar{N}$ measurements assigned to bin j.

In the low signal limit, and provided that the molecular coordinates do not change significantly during the integration period, the binomial conditions are approximately satisfied: 1), there are $\bar{N}$ trials; 2), each trial leads to either success (assignment to bin j) or failure (assignment to a bin other than j); 3), the probability of success p_j is constant over the integration period; and 4), each measurement is statistically independent. The probability distribution function is then given by

$$P_j(N_j) = p_j^{N_j}(1 - p_j)^{\bar{N}-N_j}\frac{\bar{N}!}{N_j!(\bar{N} - N_j)!}. \quad \text{(B2)}$$

Using the statistical properties of the binomial distribution, we compute the mean number of photons assigned to bin j, $\langle N_j \rangle = p_j\bar{N}$, and the variance, $\sigma^2(N_j) = p_j(1 - p_j)\bar{N}$.
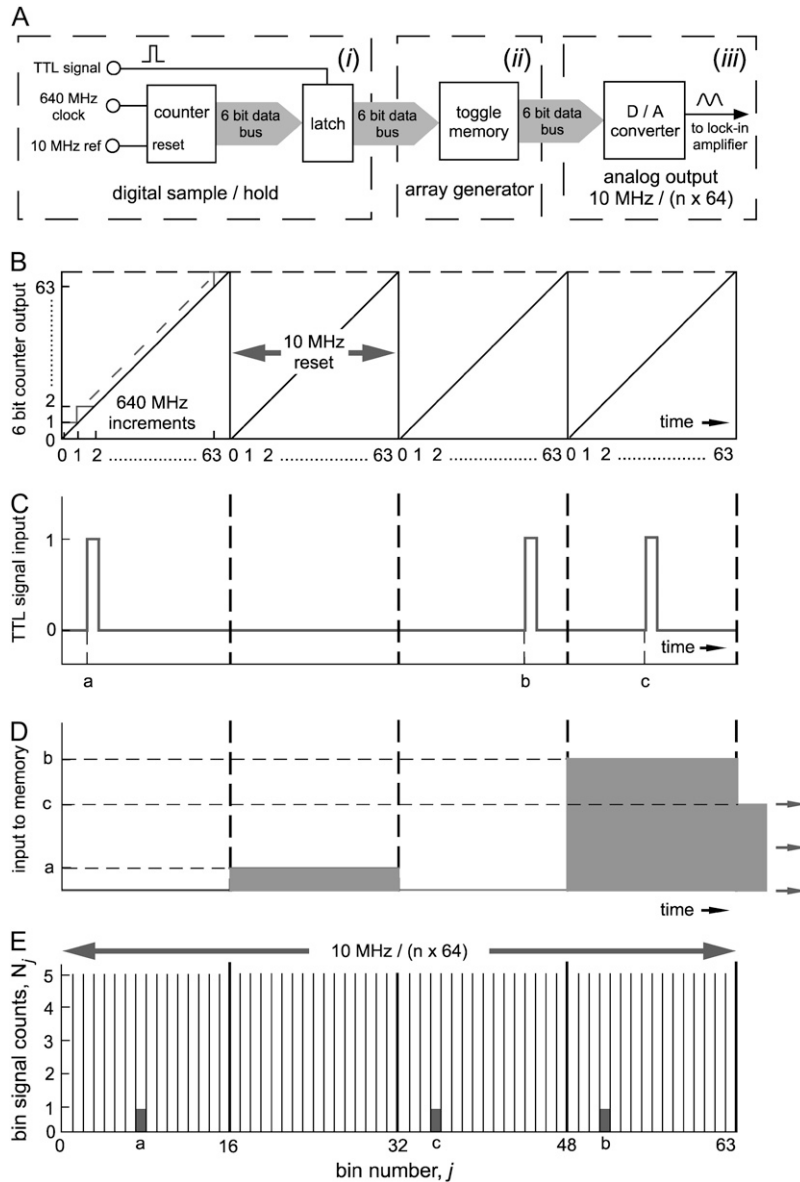
FIGURE 9 Schematic diagrams (A–E) depicting the function of the time-of-flight histogram generator (described fully in Appendix B).

Substitution of Eq. 14 into Eq. B1 leads to

$$p_j = \frac{1}{m}\left\{ 1 + \frac{|\hat{F}|}{\hat{F}(0)}\cos(\phi_j + \gamma) \right\} = \frac{1}{m}(1 + A_j), \qquad \text{(B3)}$$

where we have defined the variable $A_j = |\hat{F}|\cos(\phi_j + \gamma)/\hat{F}(0)$. We thus obtain

$$\langle N_j \rangle = \bar{N}\left(\frac{1 + A_j}{m} \right) \text{ and } \sigma^2(N_j) = \bar{N}\left(\frac{1 + A_j}{m} \right)\left[1 - \left(\frac{1 + A_j}{m} \right) \right]$$

$$\text{(B4)}$$

with signal/noise associated with bin j,

$$\frac{S}{N}(N_j) \propto \frac{\langle N_j \rangle}{\sigma(N_j)} = \sqrt{\bar{N}\Big/\left[\left(\frac{m}{1 + A_j} \right) - 1 \right]}. \qquad \text{(B5)}$$

From Eq. B5, we see that the signal/noise ratio of the jth bin scales as $\sqrt{\bar{N}}$, but is reduced by the factor $1/\sqrt{|m/(1 + A_j)| - 1}$, which accounts for the partitioning of the photons among the remaining $m - 1$ bins, and the contrast ratio proportional to the amplitude of the modulation at bin j, $|A_j|$.

To determine the average signal/noise associated with the final smoothed histogram, we sum the values of $\langle N_j \rangle$ and $\sigma^2(N_j)$, given by the expressions in Eq. B4, over the full range, i.e., $\sum_{j=0}^{m}\langle N_j \rangle = \bar{N}$ and $\sum_{j=0}^{m}\sigma^2(N_j) = \bar{N}$, such that $S/N \propto \sqrt{\bar{N}}$.

REFERENCES

1. Alberts, B., A. Johnson, J. Lewis, M. Raff, K. Roberts, and P. Walter. 2002. Molecular Biology of the Cell, 4th Ed. Garland Science, New York.

2. Alberts, B. 1998. The cell as a collection of protein machines: preparing the next generation of molecular biologists. *Cell.* 92:291–294.

3. Luby-Phelps, K. 1994. Physical properties of the cytoplasm. *Curr. Opin. Cell Biol.* 6:3–9.

4. Luby-Phelps, K. 2000. Cytoarchitecture and physical properties of cytoplasm: volume, viscosity, diffusion, intracellular surface area. *Int. Rev. Cytol.* 192:189–221.

5. Ritchie, K., R. Iino, T. Fujiwara, K. Murase, and A. Kusumi. 2003. The fence and picket structure of the plasma membrane of live cells as revealed by single molecule techniques. *Mol. Membr. Biol.* 20:13–18.

6. Douglass, A. D., and R. D. Vale. 2005. Single-molecule microscopy reveals plasma membrane microdomains created by protein-protein networks that exclude or trap signaling molecules in T cells. *Cell.* 121: 937–950.

7. Yu, J., J. Xiao, X. Ren, K. Lao, and X. S. Xie. 2006. Probing gene expression in live cells, one protein molecule at a time. *Science.* 311: 1600–1603.

8. Iino, R., I. Koyama, and A. Kusumi. 2001. Single molecule imaging of green fluorescent proteins in living cells: E-Cadherin forms oligomers on the free cell surface. *Biophys. J.* 80:2667–2677.

9. Lommerse, P. H. M., B. E. Snaar-Jagalska, H. P. Spaink, and T. Schmidt. 2005. Single-molecule diffusion measurements of H-Ras at the plasma membrane of live cells reveal microdomain localization upon activation. *J. Cell Sci.* 118:1799–1809.

10. Lawson, J. L., and G. E. Uhlenbeck. 1950. Threshold Signals. McGraw Hill, New York.

11. Baird, G. S., D. A. Zacharias, and R. Y. Tsien. 2000. Biochemistry, mutagenesis, and oligomerization of DsRed, a red fluorescent protein from coral. *Proc. Natl. Acad. Sci. USA.* 97:11984–11989.

12. Gross, L. A., G. S. Baird, R. C. Hoffman, K. K. Baldridge, and R. Y. Tsien. 2000. The structure of the chromophore within DsRed, a red fluorescent protein from coral. *Proc. Natl. Acad. Sci. USA.* 97:11990–11995.

13. Yarbrough, D., R. M. Wachter, K. Kallio, M. V. Matz, and S. J. Remington. 2001. Refined crystal structure of DsRed, a red fluorescent protein from coral, at 2.0 Å resolution. *Proc. Natl. Acad. Sci. USA.* 98:462–467.

14. Shaner, N. C., R. E. Campbell, P. A. Steinbach, B. N. G. Giepmans, A. E. Palmer, and R. Y. Tsien. 2004. Improved monomeric red, orange, and yellow fluorescent proteins derived from *Discosoma sp.* red fluorescent protein. *Nat. Biotechnol.* 22:1567–1572.

15. Margineantu, D., R. A. Capaldi, and A. H. Marcus. 2000. Dynamics of the mitochondrial reticulum in live cells using Fourier imaging correlation spectroscopy and digital video microscopy. *Biophys. J.* 79: 1833–1849.

16. Grassman, T. J., M. K. Knowles, and A. H. Marcus. 2000. Structure and dynamics of fluorescently labeled complex fluids by Fourier imaging correlation spectroscopy. *Phys. Rev. E.* 62:8245–8257.

17. Knowles, M. K., T. J. Grassman, and A. H. Marcus. 2000. Measurement of the dynamic structure function of fluorescently labeled complex fluids by Fourier imaging correlation spectroscopy. *Phys. Rev. Lett.* 85:2837–2840.

18. Knowles, M. K., D. Margineantu, R. A. Capaldi, and A. H. Marcus. 2002. Translational dynamics of fluorescently labeled species by Fourier imaging correlation spectroscopy. *In* Liquid Dynamics: Experiment, Simulation and Theory. J. T. Fourkas, Editor. American Chemical Society, Washington, DC.

19. Knowles, M. K., A. R. Honerkamp-Smith, and A. H. Marcus.2005. Direct measurement of relative and collective diffusion in a dilute binary colloidal suspension. *J. Chem. Phys.* 122:234909-1–234909-13.

20. Lounis, B., J. Deich, F. I. Rosell, S. G. Boxer, and W. E. Moerner. 2001. Photophysics of DsRed, a red fluorescent protein, from the ensemble to the single-molecule level. *J. Phys. Chem. B.* 105:5048–5054.

21. Heikal, A. A., S. T. Hess, G. S. Baird, R. Y. Tsien, and W. W. Webb. 2000. Molecular spectroscopy and dynamics of intrinsically fluorescent proteins: coral red (DsRed) and yellow (Citrine). *Proc. Natl. Acad. Sci. USA.* 97:11996–12001.

22. Malvezzi-Campeggi, F., M. Jahnz, K. G. Heinze, P. Dittrich, and P. Schwille. 2001. Light-induced flickering of DsRed provides evidence for distinct and interconvertible fluorescent states. *Biophys. J.* 81:1776–1785.

23. Mazo, R. M. 2002. Brownian motion: fluctuations, dynamics and applications. *In* International Series of Monographs on Physics, Vol. 112, 1st Ed. Oxford Science Publications, Oxford, UK.

24. Hansen, J.-P., and I. R. McDonald. 1986. Theory of Simple Liquids. Academic Press, San Diego.

25. Berne, B. J., and R. Pecora. 1976. Dynamic Light Scattering. Krieger, Malabar, FL.

26. Pusey, P. N., and R. J. A. Tough. 1985. Particle interactions. *In* Dynamic Light Scattering: Applications of Photon Correlation Spectroscopy. R. Pecora, Editor. Plenum Press, New York.

27. Ediger, M. D., C. A. Angell, and S. R. Nagel. 1996. Supercooled liquids and glasses. *J. Phys. Chem.* 100:13200–13212.

28. Pusey, P. N., H. M. Fijnaut, and A. Vrij. 1982. Mode amplitudes in dynamic light scattering by concentrated liquid suspensions of polydisperse hard spheres. *J. Chem. Phys.* 77:4270–4281.

29. Brown, J. C., P. N. Pusey, and R. Dietz. 1975. Photon correlation study of polydisperse samples of polystyrene in cyclohexane. *J. Chem. Phys.* 62:1136–1144.

30. Koppel, D. E. 1972. Analysis of macromolecular polydispersity in intensity correlation spectroscopy: the method of cumulants. *J. Chem. Phys.* 57:4814–4820.

31. Davoust, J., P. F. Devaux, and L. Leger. 1982. Fringe pattern photobleaching, a new method for the measurement of transport coefficients of biological macromolecules. *EMBO J.* 1:1233–1238.

32. Fink, M. C. 2006. Molecular Fourier imaging correlation spectroscopy to studies of molecular diffusion. *In* Chemistry. University of Oregon, Eugene, OR.

33. Bowen, B., and N. Woodbury. 2003. Single-molecule fluorescence lifetime and anisotropy measurements of the red fluorescent protein, DsRed, in solution. *Photochem. Photobiol.* 77:362–369.

34. Aragon, S. R., and R. Pecora. 1976. Fluorescence correlation spectroscopy as a probe of molecular dynamics. *J. Chem. Phys.* 64:1791–1803.

35. Aragon, S. R., and R. Pecora. 1975. Fluorescence correlation spectroscopy and Brownian rotational diffusion. *Biopolymers.* 14:119–138.

36. Axelrod, D. 1989. Fluorescence polarization microscopy. *Methods Cell Biol.* 30:333–352.

37. Axelrod, D. 1979. Carbocyanine dye orientation in red cell membrane studied by microscopic fluorescence polarization. *Biophys. J.* 26:557–574.

38. Lakowicz, J. R. 1983. Principles of Fluorescence Spectroscopy. Plenum Press, New York.

39. Horowitz, P., and W. Hill. 1986. The Art of Electronics. Cambridge University Press, New York.

40. Schwille, P., S. Kummer, A. A. Heikal, W. E. Moerner, and W. W. Webb. 2000. Fluorescence correlation spectroscopy reveals fast optical excitation-driven intramolecular dynamics of yellow fluorescent proteins. *Proc. Natl. Acad. Sci. USA.* 97:151–156.

41. Bonsma, S., J. Gallus, F. Konz, R. Purchase, and S. Volker. 2004. Light-induced conformational changes and energy transfer in red fluorescent protein. *J. Luminesc.* 107:203–212.

42. Creemers, T. M. H., A. J. Lock, V. Subramaniam, T. M. Jovin, and S. Volker. 2000. Photophysics and optical switching in green fluorescent protein mutants. *Proc. Natl. Acad. Sci. USA.* 97:2974–2978.

43. Creemers, T. M. H., A. J. Lock, V. Subramaniam, T. M. Jovin, and S. Volker. 2002. Red-shifted mutants of green fluorescent protein: reversible photoconversions studied by hole-burning and high-resolution spectroscopy. *Chem. Phys.* 275:109–121.

44. Konz, F., R. Purchase, S. Bonsma, J. Gallus, and S. Volker. 2004. Optical dephasing in red fluorescent protein. *J. Luminesc.* 108: 153–157.

45. Schwille, P., S. Kummer, A. A. Heikal, W. E. Moerner, and W. W. Webb. 2000. Fluorescence correlation spectroscopy reveals fast optical excitation-driven intramolecular dynamics of yellow fluorescence proteins. *Proc. Natl. Acad. Sci. USA*. 97:151–156.

46. Cantor, C. R., and P. R. Schimmel. 1980. Biophysical Chemistry: Techniques for the Study of Biological Structure and Function, Vol. II. W. H. Freeman, New York.

47. Weast, R. C. 1983. CRC Handbook of Chemistry and Physics. CRC Press, Boca Raton, FL.

48. Phillies, G. D. J. 2005. Interpretation of light-scattering spectra in terms of particle displacements. *J. Chem. Phys*. 122:224905-1–224905-8.

49. Glotzer, S. C. 2000. Spatially heterogeneous dynamics in liquids: insights from simulation. *J. Non-Cryst. Sol*. 274:342–355.

50. Richert, R. 2002. Heterogeneous dynamics in liquids: fluctuations in space and time. *J. Phys. Condens. Matter*. 14:R703–R738.

51. Deschenes, L. A., and D. A. Vanden Bout. 2001. Single-molecule studies of heterogeneous dynamics in polymer melts near the glass transition. *Science*. 292:255–258.

52. Behrends, R., K. Fuchs, U. Kaatze, Y. Hayashi, and Y. Feldman. 2006. Dielectric properties of glycerol/water mixtures at temperatures between 10 and 50°C. *J. Chem. Phys*. 124:144512-1–144512-8.

53. Sudo, S., M. Shimomura, N. Shinyashiki, and S. Yagihara. 2002. Broadband dielectric study of α-β separation for supercooled glycerol-water mixtures. *J. Non-Cryst. Sol*. 307–310:356–363.

54. Boon, J. P., and S. Yip. 1980. Molecular Hydrodynamics. Dover Publications, New York.